Synchrotron radiation reveals transient weakening during mineral phase transformations

Andrew J. Cross[1]*, Rellie M. Goddard[1,2], Kathryn M. Kumamoto[3], David L. Goldsby[4], Lars N. Hansen[5], Haiyan Chen[6], Diede Hein[5], Christopher A. Thom[7], M. Adaire Nehring[5]

[1] Department of Geology and Geophysics, Woods Hole Oceanographic Institution; Woods Hole, MA 02532, USA
[2] Department of Geology, Lakehead University; Thunder Bay, ON, P7B 5E1, Canada
[3] Lawrence Livermore National Laboratory; Livermore, CA 94550, USA
[4] Department of Earth and Environmental Science, University of Pennsylvania; Philadelphia, PA 19104, USA
[5] Department of Earth and Environmental Sciences, University of Minnesota Twin Cities; Minneapolis, MN 55455, USA
[6] Mineral Physics Institute, Stony Brook University; Stony Brook, NY 11794, USA
[7] Rhenium Alloys, Inc.; North Ridgeville, OH 44035, USA

*Corresponding author. Email: across@whoi.edu

Abstract

Phase transformations are widely invoked as a source of rheological weakening during subduction, continental collision, mantle convection, and various other geodynamic phenomena. However, the likelihood and magnitude of such weakening in nature remains undetermined. Here, experiments performed on a synchrotron beamline reveal dramatic weakening across the polymorphic quartz↔coesite phase transition. Under non-hydrostatic conditions, we observe a transient decrease in effective viscosity of up to two orders of magnitude. Such weakening occurs only when the transformation outpaces deformation. We suggest that this behavior is broadly applicable among silicate minerals and examine the likelihood of slab weakening due to the olivine-spinel phase transformation. Our model suggests that cold, wet slabs are most susceptible to transformational weakening, consistent with geophysical observations of slab stagnation beneath the western Pacific.

Main Text

Rocks and minerals undergo a myriad of solid-state phase transformations during their burial and exhumation through Earth's interior. Notable examples include the transition from quartz to coesite during continental collision, olivine to spinel within the mantle transition zone, and perovskite to post-perovskite near the core-mantle boundary. Such transitions are thought to produce mechanical weakening through various processes. For example, rapid changes in volume (*1*) and elastic properties (*2*) can generate internal stresses large enough to induce brittle damage, a potential mechanism for nucleating deep-focus earthquakes (*1*, *3*). Phase transformations can also cause rheological weakening under conditions that preclude brittle failure. Of particular interest are the phenomena of structural superplasticity and transformation

plasticity. Structural superplasticity (*i.e.*, grain-size sensitive creep) arises from the formation of fine-grained transformation products that impart long-lived weakening (*4*, *5*). Transformation plasticity on the other hand, though often loosely defined, involves transient weakening during a solid-state phase transformation (*6*–*9*), manifested either as a strain rate increase (*10*) or as a stress drop (*11*). However, various other characteristics have been attributed to transformation plasticity, including: 'excess' plastic deformation produced during a phase transformation, even when the applied stress does not exceed the yield stress (*6*, *8*, *12*); anisotropy of the transformation volume change (*13*); and proportionality between the magnitude of excess straining and the applied stress, volume change, and transformation kinetics (*6*, *9*). Such effects are commonly ascribed to dislocation flux driven by internal stress heterogeneity.

Transformation plasticity has been invoked across a variety of geodynamic contexts—including mantle convection (*14*, *15*), subduction (*16*, *17*), crustal deformation (*9*, *18*), and mantle plume upwelling (*7*)—and has even been suggested as perhaps *"the primary deformation mechanism in the crust as well as in most of the upper mantle between 400 and 800 km"* (*9*). Nevertheless, transformation plasticity has proven difficult to examine in the laboratory due to the technical challenges associated with resolving transient effects *in situ*, particularly at elevated temperatures and pressures. As such, most experimental studies to date have focused on phase transformations that occur at ambient pressure (*10*, *13*, *19*, *20*), often in rock analogs (*8*, *11*, *21*).

To explore the transient rheological effects of phase transformations at more Earth-relevant conditions, deformation-DIA (D-DIA) experiments were performed on a synchrotron beamline to examine the quartz↔coesite (SiO_2) phase transition *in situ*. We chose to study SiO_2 for three primary reasons: first, its abundance in Earth's crust; second, the relative accessibility of the

quartz↔coesite transition; and third, as a model (analog) system for other silicate minerals (e.g., olivine). Two types of experiment were performed. In hydrostatic (control) runs, SiO_2 samples were pressurized from the quartz to the coesite stability field under isothermal conditions. Confining pressure, differential stress, and mineral phase proportions were monitored continuously using energy dispersive X-ray diffraction (XRD), while axial and volumetric strain were measured via X-ray radiography (see *Materials and Methods* for full details). After the sample had fully transformed to coesite, pressure was lowered to induce the reverse, coesite-to-quartz phase transformation. In non-hydrostatic (test) runs, the same procedure was followed while simultaneously deforming the sample via uniaxial shortening. Non-hydrostatic experiments were performed at various temperatures and deformation rates (Table S1). As a reference standard and stress sensor, each experimental assembly also contained a fine-grained, polycrystalline aggregate of San Carlos olivine (Fo_{90}), which did not undergo a phase transformation over the range of experimental conditions explored here. The experiment procedure is detailed in the *Materials and Methods*.

Results

Fig. 1 shows the mechanical evolution of our samples when pressure-cycled across the quartz↔coesite phase transition under hydrostatic versus non-hydrostatic conditions. Under hydrostatic conditions, the Fo_{90} reference standard undergoes a gradual volume reduction of 3.7% during pressurization from the quartz to coesite stability fields (Fig. 1G, green triangles). This volume reduction is almost completely reversed during decompression back to the quartz stability field—a small (<1%) residual volumetric strain can be accounted for entirely by elastic effects, considering the difference between the initial and final confining pressures (Fig. 1A). The Fo_{90} volume change is isotropic, such that sample shape remains constant throughout the

experiment (Fig. 1I). Initially, the SiO_2 sample undergoes a similar gradual volume reduction during pressurization, though larger in magnitude due to the greater compressibility (*i.e.*, smaller bulk modulus) of quartz. However, upon reaching a confining pressure of 3–4 GPa, there is a sharp reduction in volume of ~6% (Fig. 1G, orange squares) coinciding with the emergence of coesite XRD peaks and concomitant loss of quartz XRD peaks (Fig. 1L). During this period, differential stress decreases by 400–500 MPa, placing the sample in deviatoric tension along the vertical axis. Meanwhile, the phase transition introduces a small flattening strain (Fig. 1I) with 50% of the SiO_2 volume change accommodated along the vertical axis (greater than the 33% axial strain expected for a perfectly isotropic volume change). Nevertheless, this flattening strain is reversed upon passing back through the coesite-to-quartz phase transition (Fig. 1I), producing no net change in sample shape and only a small residual axial strain (~2%; Fig. 1E) and volumetric strain (~2%; Fig. 1G). We likewise attribute these residual strains to the difference in confining pressure between the start and end of the experiment.

Fig. 1. Mechanical evolution under hydrostatic versus non-hydrostatic conditions. (**A–B**) Confining pressure, σ_3, (**C–D**) differential stress, $\sigma_1 - \sigma_3$, (**E–F**) axial strain, (**G–H**) volumetric strain, (**I–J**) sample aspect ratio (diameter divided by height) relative to the initial sample shape, and (**L–K**) coesite volume proportion as a function of time, calculated from the relative intensities of quartz and coesite diffraction peaks (see *Materials and Methods*). Vertical gray bars represent the time intervals over which both quartz and coesite peaks are present in the XRD spectra. Orange squares and green triangles represent the SiO_2 sample and Fo_{90} reference standard, respectively, in (**E–J**).

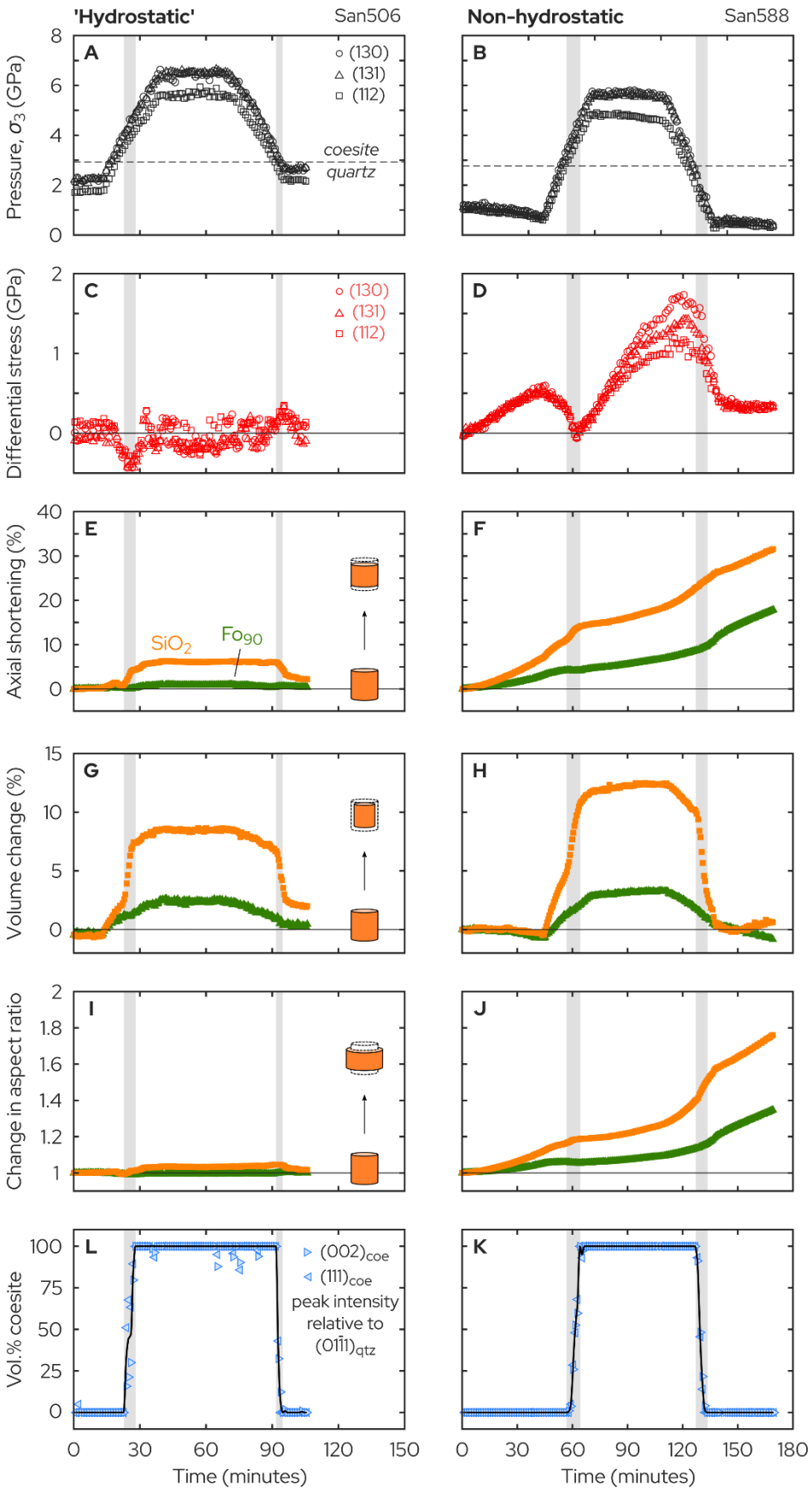
'Hydrostatic'
San506
Non-hydrostatic
San588
A
B
C
D
E
F
G
H
I
J
K
L
Pressure, σ3 (GPa)
Differential stress (GPa)
Axial shortening (%)
Volume change (%)
Change in aspect ratio
Vol.% coesite
(130)
(131)
(112)
coesite
quartz
SiO2
Fo90
(002)coe
(111)coe
peak intensity relative to (01$\bar{1}$1)qtz
Time (minutes)
Time (minutes)

105

Under non-hydrostatic conditions, both the SiO_2 and Fo_{90} samples undergo continuous isochoric flattening due to the imposed uniaxial shortening (Figs. 1F, 1J). A steady-state strain rate of 4.5 $\times 10^{-5}$ s^{-1} is reached in the quartz sample after ~4% axial shortening, while differential stress continues to increase into the range of several hundred MPa. After reaching an axial strain of 8%, we start increasing confining pressure to induce the quartz-to-coesite phase transition. As before, the phase transition produces a rapid ~6% volume decrease in the SiO_2 sample (Fig. 1H), 50% of which is accommodated along the compression axis (Fig. 1F). At the same time, the applied differential stress completely relaxes, placing the sample under a deviatoric tensional stress of 50–60 MPa along the compression axis at the mid-point of the phase transition (Fig. 1B). Thereafter, differential stress begins increasing to place the sample back into a compressive stress regime, approaching a steady-state value of 1.0–1.5 GPa in the coesite stability field.

The most marked differences between the hydrostatic and non-hydrostatic experiments are observed during depressurization and the associated coesite-to-quartz transition. Whereas the SiO_2 sample became unflattened during depressurization in the hydrostatic experiment (Fig. 1E), we observe significant additional flattening during the non-hydrostatic coesite-to-quartz transition (Fig. 1J), despite the sharp increase in sample volume (Fig. 1H). X-ray radiographs reveal that the SiO_2 sample—instead of lengthening, as in the hydrostatic experiment—accommodates the volume increase by expanding perpendicular to the compression axis (*i.e.*, parallel to the minimum principal stress, σ_3, axis). This observation is common to all of our non-hydrostatic experiments and reflects a “biasing” (anisotropy) of the volume change due to the presence of a differential stress, which, in this case, relaxes gradually by ~1 GPa during the coesite-quartz transition, remaining compressive throughout (Fig. 1D). Interestingly, the Fo_{90} reference standard begins deforming five times faster towards the end of the coesite-quartz

transition, before returning to a lower strain rate in the quartz stability field (Fig. 1F). Again, this observation is common among our non-hydrostatic experiments, and is attributed to internal stresses generated by the SiO_2 volume increase within our deformation assembly (in effect, the SiO_2 sample pushing against the Fo_{90} sample as it expands). Internal stresses may also explain the lack of a dramatic stress drop during the coesite-to-quartz transition, such as that seen during the quartz-to-coesite transition.

To assess the effect of deformation conditions on the magnitude of transient weakening, we performed non-hydrostatic experiments at nominal temperatures in the range 800–950°C, and differential ram displacement rates corresponding to SiO_2 axial strain rates in the range 10^{-7}–10^{-4} s^{-1} (see *Materials and Methods*). Fig. 2 shows SiO_2 sample viscosity as a function of time, alongside the volume proportion of coesite through time. During the quartz→coesite transformation, we observe marked transient weakening under most conditions, manifested as a short-lived decrease in SiO_2 sample viscosity (*e.g.*, Fig. 2A). These viscosity drops coincide with the point at which there is a roughly 50-50 vol.% mixture of quartz and coesite—in other words, the point at which the phase transformation is proceeding most rapidly. While the magnitude of transient weakening is not clearly temperature-dependent—compare, for example, Figs. 2A, C, and F——we do observe a strong strain-rate dependence. At the lowest deformation rate (0.0003 mm/s differential ram syringe pump rate), the SiO_2 sample becomes 1–2 orders of magnitude weaker during the quartz→coesite transition (Figs. 2, left column), whereas scarcely any weakening is detected at the highest deformation rate (0.01 mm/s differential ram syringe pump rate; Figs. 2, right column). The reverse, coesite→quartz transformation, on the other hand, produces no significant or systematic change in viscosity in most experiments. One notable exception is experiment San574, conducted at the highest temperature and lowest strain rate, in

which the coesite→quartz transformation produces more than a tenfold reduction in viscosity (Fig. 2F). In this experiment, the sample went into deviatoric tension during the quartz→coesite transformation, and back to deviatoric compression during the coesite→quartz transformation—the observed viscosity drops reflect these changes between positive to negative differential stresses (*i.e.*, passing through zero differential stress).

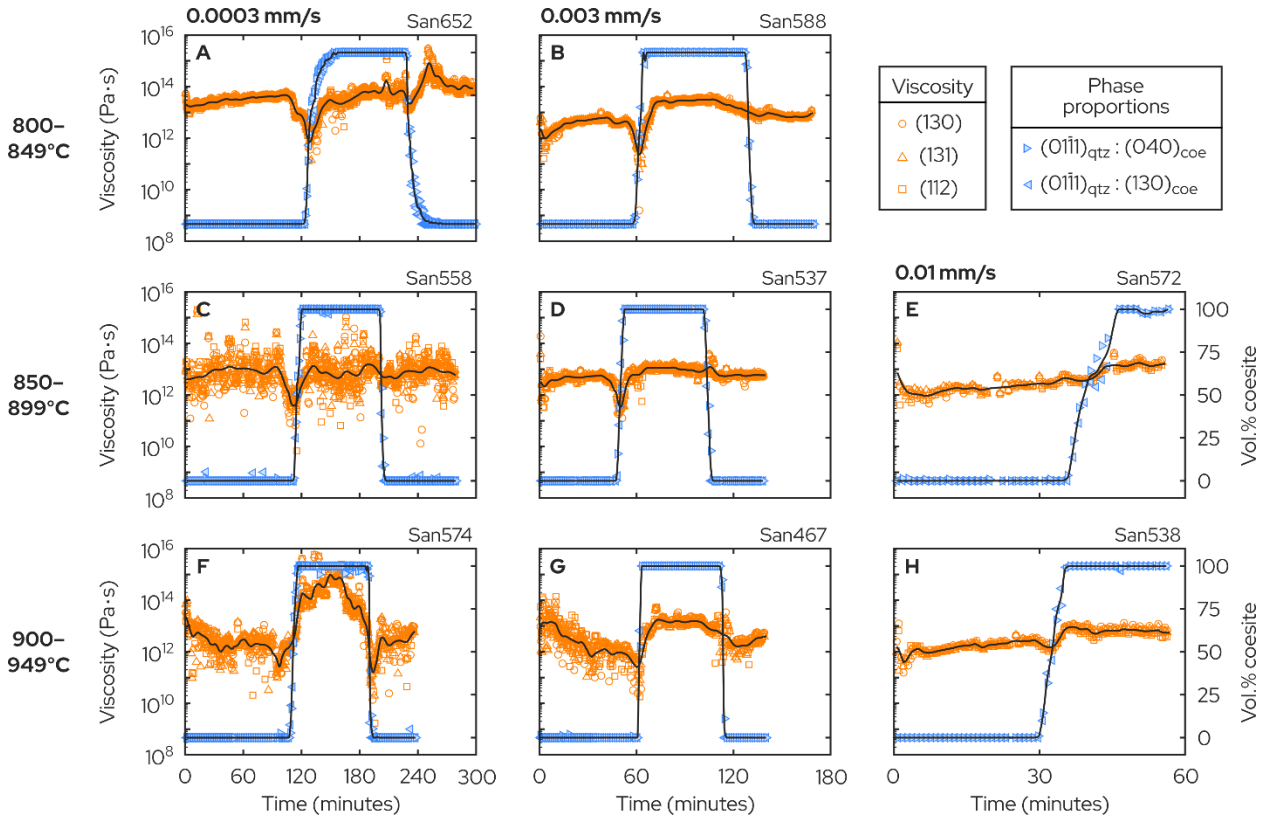

Fig. 2. Viscosity evolution as a function of temperature (top to bottom) and deformation rate (left to right). Each experiment was performed under a nominally constant temperature within the indicated ranges. Viscosity (orange symbols) is calculated from the first time-derivative of the SiO_2 axial strain (*i.e.*, strain rate) and differential stress from three diffraction peaks in the Fo_{90} stress sensor: (130), (131), and (112). As a visual aid, a spline has been fit through the average of these data (black curve). Also shown (blue symbols) are the volume proportions of coesite as a function of time, calculated from the relative heights of the (040) and (130) XRD peaks in coesite and the $(01\bar{1}1)$ peak in quartz (see *Materials and Methods*).

Discussion

We propose that transformation-induced weakening in our experiments is primarily governed by a competition between the imposed rate of deformation and the induced rate of phase transformation. Weakening occurs when the phase transformation is rapid relative to the imposed deformation (*i.e.*, at low differential ram rates and strain rates; Figs 2A–F), whereas no weakening occurs when deformation is able to keep pace with the transformation (*i.e.*, at high differential ram rates and strain rates; Figs. 2G–H). Weakening thus arises from an effective (additional) strain rate produced as the sample passes through the phase transition and undergoes a change in volume—an effect predicted by Poirier (*9*) in a theoretical treatment of transformation plasticity. We illustrate this effect in Fig. 3 by plotting the magnitude of transient weakening, F_W, versus a rate factor, F_R, defined as the ratio between the transformation rate and deformation rate—see the *Supplementary Text* for detailed descriptions. In short, F_W represents the amplitude of the quartz→coesite viscosity drop for each experiment, while F_R is taken as the ratio of the transformation rate (*i.e.*, volumetric strain rate resolved along the compression direction) and deformation rate (*i.e.*, ambient axial strain rate)—see Fig. S6 for a schematic illustration. Both quantities are dimensionless. As expected, weakening occurs only when $F_R > 1$, becoming more pronounced (*i.e.*, increasing F_W) as the transformation increasingly outpaces deformation (*i.e.*, increasing F_R). We note that most experiments fall on a linear trend lying above the 1:1 line between F_W and F_R (Fig. 3). The 1:1 line represents the amount of weakening expected solely from the effective increase in strain rate (due to the volume change)—for instance, if the volume change produces an effective tenfold increase in strain rate along the compression direction, the sample must, by definition, experience a tenfold transient decrease in viscosity. The additional weakening revealed by Fig. 3 arises, at least in part if not entirely, from elastic unloading of the sample as it contracts, causing differential stress to decrease (*e.g.*, Figs.

1C–D; (*22*)) as observed and ascribed to transformation plasticity in experiments on cobalt (*11*). Other potential sources of weakening are transformational faulting (*1*), grain size reduction (*5*), and dislocation nucleation and glide driven by transformation-induced internal stresses (*9*). Experiments to quantify microstructure evolution across the quartz↔coesite transition are underway and will be presented at a later date. For now, we examine two experimental samples quenched mid-way through the quartz→coesite phase transition: one at ~800°C (San552) and the other at ~900°C (San568), both under non-hydrostatic conditions with 0.003 mm/s differential ram syringe pump rate (Table S1). Backscattered electron images reveal that the samples have undergone 50–90% of the transformation to coesite (Fig. S7). Remnant quartz grains are equant and fine-grained (1–10 µm diameter at 800°C, 10–30 µm diameter at 900°C), whereas coesite forms large needle- (San552; Fig. S7a) or lath-shaped (San568; Fig. S7b) grains, up to 200 µm in length and with aspect ratios frequently >10. Clearly, weakening cannot be explained by grain-size reduction in our experiments. We also do not find any evidence for transformational faulting—only sample San552 contains visible, horizontal cracks, which we attribute to decompression at the end of the experiment. Dislocation analyses are beyond the scope of this study; however, we reiterate that weakening is not strongly temperature-dependent (Figs. 2 and 3), which might imply that dislocations play a limited role, given the expected temperature dependence of dislocation recovery (*18*).

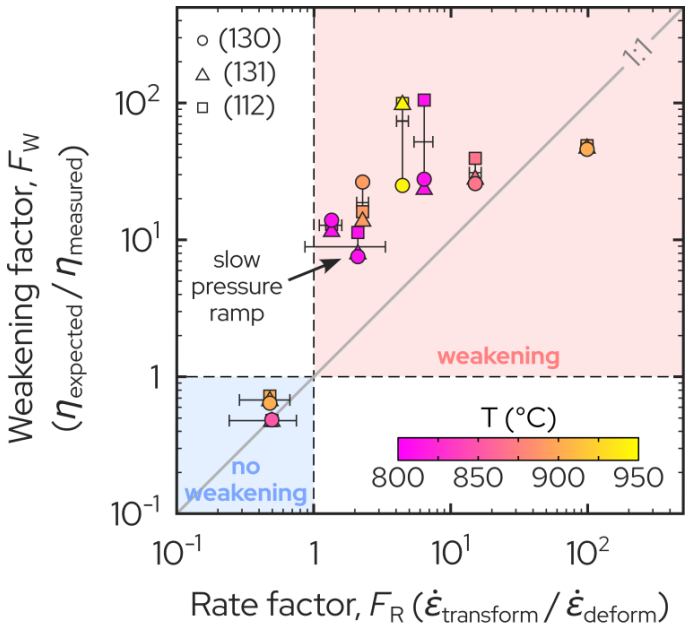

Fig. 3. Magnitude of transient weakening, F_W, versus the ratio between the rates of transformation and deformation, F_R. See text for details. Three weakening factors are calculated for each experiment, one for each Fo_{90} diffraction peak. Rate factor errors are calculated assuming conservative uncertainties on the transformation rate, $\Delta\dot{\varepsilon}_{transform}$, and deformation rate, $\Delta\dot{\varepsilon}_{deform}$ (see *Supplementary Text*). Data points are colored according to experiment temperature.

To assess how our observations scale to longer (geologic) timescales, we performed one experiment where pressure was ramped an order of magnitude slower than in all other experiments (San585; Table S1; Fig. S8, middle column). As with all other non-hydrostatic experiments, the sample experienced a rapid stress drop (Fig. S8E) and transient strain-rate increase (Fig. S8H) during the quartz→coesite transformation. The only significant difference is the occurrence of a double viscosity drop (Fig. S8Q) due to the sample passing twice through the point of zero differential stress: first as the stress state changes from deviatoric compression to tension near the onset of the transformation, then back to compression upon the completion of the transformation. Crucially, the magnitude of weakening observed in San585 is entirely consistent with our other experiments, plotting on the same trend of F_W versus F_R (Fig. 3).

Having established a scalable rate parameter, F_R, we now seek to interrogate whether phase transformations can produce similar weakening on geologic timescales. As an example, we consider the case of a slab passing through Earth's mantle transition zone, assuming that our findings for SiO_2 are applicable to other mineral systems. Following Hosoya *et al.* (*23*), we calculate the progression of the olivine-wadsleyite phase transformation for a slab being subducted at a rate of 12 cm/yr, with a thermal gradient of 0.6°C/km, and 5 mm olivine grain size. We vary slab temperature at the 660-km discontinuity between 600°C and 1200°C, representing the range of cold to hot subduction zones (*24*), while water content is varied between 1 and 10,000 wt. ppm H_2O to encompass dry to water-saturated conditions (*25*). The transformation rate, $\dot{\varepsilon}_{transform}$, is taken as one-third of the maximum volumetric strain rate for each set of slab conditions, assuming an isotropic, 10% total volume reduction from olivine to wadsleyite (Fig. S9A). Meanwhile, we calculate slab deformation using rheological flow laws for wet dislocation creep and low-temperature plasticity of olivine (*26*, *27*) for slab stresses up to 300 MPa (*28*–*30*). The deformation rate, $\dot{\varepsilon}_{deform}$, is taken as the total strain rate at the same depth as $\dot{\varepsilon}_{transform}$ for each set of conditions (Fig. S9B). We neglect the role of intracrystalline (martensitic) nucleation for the olivine-spinel transformation, which is thought to proceed more rapidly than intercrystalline (diffusional) nucleation and growth (*30*). Thus, our model provides a lower bound on F_R (by underestimating $\dot{\varepsilon}_{transform}$). A detailed description of the model is provided in the *Supplementary Text*.

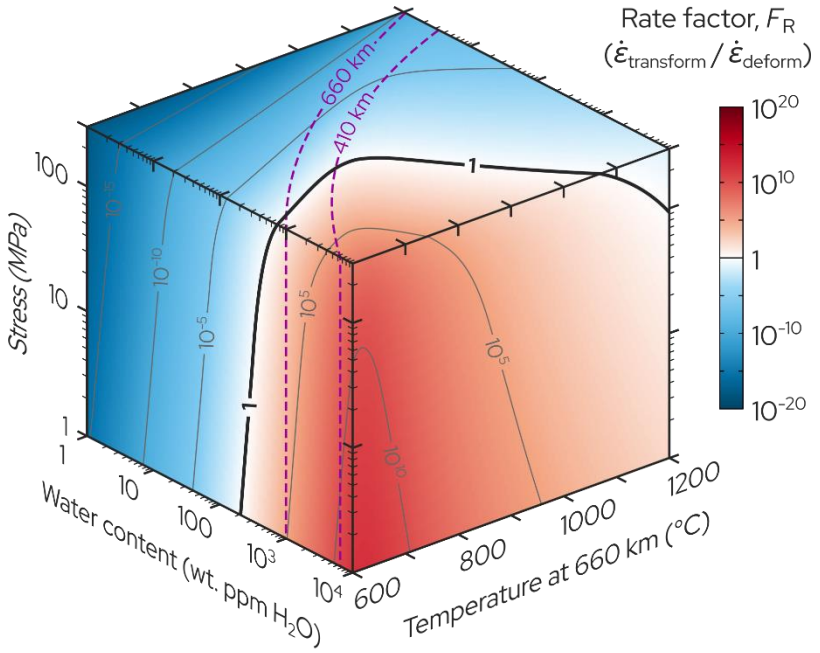

Fig. 4. Transformation rate factor, F_R, as a function of water content, temperature, and stress in a subducting slab. Transient weakening occurs when $F_R > 1$ (white to red shading). Dashed lines indicate the range of conditions over which the maximum transformation rate (*i.e.*, the point of maximum weakening) coincides with the mantle transition zone (410–660 km depth).

Fig. 4 shows the rate factor, F_R, as a function of water content, temperature, and stress in a downgoing slab. Due to the highly non-linear nature of both the phase transformation kinetics and rheological behavior, F_R varies over 30 orders of magnitude, from 10^{-18} to 10^{12} for the range of conditions explored here. Crucially, we find a large swath of parameter space over which $F_R >$ 1—indicating conditions favorable for transient, transformation-induced weakening of the type seen in our experiments—with more weakening predicted for cold, wet slabs. No weakening is predicted for slabs in which olivine contains <20 wt. ppm H_2O (<150 wt. ppm H_2O for a slab stress of 300 MPa). Furthermore, we find that the point of maximum transient weakening (*i.e.*, the depth at which the phase transformation rate is greatest) coincides with the mantle transition zone (410–660 km depth) for cold, wet slabs (Fig. 4, dashed lines). These predictions are

interesting for two reasons. First, recent water-partitioning experiments have shown that even in wet slabs, olivine will be kinetically dry (containing only ~1 wt. ppm H_2O) when coexisting with hydrous phases (*25*). Thus, transformational weakening may be triggered by water release upon the thermal breakdown of hydrous phases, with the hydration of olivine enhancing the phase transformation kinetics. Second, seismic tomography studies have revealed that some slabs buckle and stagnate within the mantle transition zone or shallow lower mantle (500–1000 km depth), particularly along the margins of the Pacific plate, where old, cold oceanic lithosphere is subducted (*31*). Slab stagnation has been ascribed to various phenomena, including heat release during phase transitions (*32*, *33*), mantle viscosity structure (*34*, *35*), trench retreat (*36*, *37*), structural superplasticity (*4*, *5*), and transformation plasticity (*15*). Our experiments demonstrate that phase transformations can indeed impart a significant, transient decrease in effective viscosity, providing mechanical instability that is consistent with geophysical observations of slab stagnation in cold, wet slabs. Thus, our results highlight the complex coupling between metamorphism and rheological behavior, and provide a quantitative basis for incorporating transformational weakening in future geodynamic simulations.

References and Notes

1. H. W. Green II, P. C. Burnley, A new self-organizing mechanism for deep-focus earthquakes. *Nature* **341**, 733–737 (1989).

2. S. E. Johnson, W. J. Song, A. C. Cook, S. S. Vel, C. C. Gerbi, The quartz $\alpha \leftrightarrow \beta$ phase transition: Does it drive damage and reaction in continental crust? *Earth Planet. Sci. Lett.* **553**, 116622 (2021).

3. J. Gasc, C. Daigre, A. Moarefvand, D. Deldicque, J. Fauconnier, B. Gardonio, C. Madonna, P. Burnley, A. Schubnel, Deep-focus earthquakes: From high-temperature experiments to cold slabs. *Geology* **50**, 1018–1022 (2022).

4. S. Karato, M. R. Riedel, D. A. Yuen, Rheological structure and deformation of subducted slabs in the mantle transition zone: implications for mantle circulation and deep earthquakes. *Phys. Earth Planet. Inter.* **127**, 83–108 (2001).

5. A. Mohiuddin, S. Karato, J. Girard, Slab weakening during the olivine to ringwoodite transition in the mantle. *Nat. Geosci.* **13**, 170–174 (2020).

6. G. W. Greenwood, R. H. Johnson, L. Rotherham, The deformation of metals under small stresses during phase transformations. *Proc. R. Soc. Lond. Ser. Math. Phys. Sci.* **283**, 403–422 (1997).

7. R. B. Gordon, Observation of crystal plasticity under high pressure with applications to the Earth's mantle. *J. Geophys. Res. 1896-1977* **76**, 1248–1254 (1971).

8. C. G. Sammis, J. L. Dein, On the possibility of transformational superplasticity in the Earth's mantle. *J. Geophys. Res. 1896-1977* **79**, 2961–2965 (1974).

9. J. P. Poirier, On transformation plasticity. *J. Geophys. Res. Solid Earth* **87**, 6791–6797 (1982).

10. A. Sauveur, What is steel? *Min. Metall.* **5**, 465–468 (1924).

11. M. Zamora, J. P. Poirier, Experiments in anisothermal transformation plasticity: The case of cobalt. Geophysical implications. *Mech. Mater.* **2**, 193–202 (1983).

12. D. C. Dunand, C. Schuh, D. L. Goldsby, Pressure-Induced Transformation Plasticity of H2O Ice. *Phys. Rev. Lett.* **86**, 668–671 (2001).

13. A. C. D. Chaklader, Deformation of Quartz Crystals at the Transformation Temperature. *Nature* **197**, 791–792 (1963).

14. D. C. Rubie, A. J. Brearley, Phase Transitions Between β and γ (Mg, Fe)2SiO4 in the Earth's Mantle: Mechanisms and Rheological Implications. *Science* **264**, 1445–1448 (1994).

15. S. V. Panasyuk, B. H. Hager, A model of transformational superplasticity in the upper mantle. *Geophys. J. Int.* **133**, 741–755 (1998).

16. L. Ruff, H. Kanamori, Seismic coupling and uncoupling at subduction zones. *Tectonophysics* **99**, 99–117 (1983).

17. W. Mao, S. Zhong, Slab stagnation due to a reduced viscosity layer beneath the mantle transition zone. *Nat. Geosci.* **11**, 876–881 (2018).

18. M. S. Paterson, Creep in transforming polycrystalline materials. *Mech. Mater.* **2**, 103–109 (1983).

19. R. S. Coe, M. S. Paterson, The α–β Inversion in quartz: A coherent phase transition under nonhydrostatic stress. *J. Geophys. Res. 1896-1977* **74**, 4921–4948 (1969).

20. P. Gillet, Y. Gérard, C. Willaime, The calcite-aragonite transition: mechanism and microstructures induced by the transformation stresses and strain. *Bull. Minéralogie* **110**, 481–496 (1987).

21. D. H. Zeuch, S. T. Montgomery, J. D. Keck, Some observations on the effects of shear stress on a polymorphic transformation in perovskite-structured lead-zirconate-titanate ceramic. *J. Geophys. Res. Solid Earth* **98**, 1901–1911 (1993).

22. Y. Zhou, C. He, J. Song, S. Ma, J. Ma, An experiment study of quartz-coesite transition at differential stress. *Chin. Sci. Bull.* **50**, 446–451 (2005).

23. T. Hosoya, T. Kubo, E. Ohtani, A. Sano, K. Funakoshi, Water controls the fields of metastable olivine in cold subducting slabs. *Geophys. Res. Lett.* **32** (2005).

24. S. H. Kirby, S. Stein, E. A. Okal, D. C. Rubie, Metastable mantle phase transformations and deep earthquakes in subducting oceanic lithosphere. *Rev. Geophys.* **34**, 261–306 (1996).

25. T. Ishii, E. Ohtani, Dry metastable olivine and slab deformation in a wet subducting slab. *Nat. Geosci.* **14**, 526–530 (2021).

26. G. Hirth, D. Kohlstedt, "Rheology of the Upper Mantle and the Mantle Wedge: A View from the Experimentalists" in *Inside the Subduction Factory* (American Geophysical Union, 2003)*Geophysical Monograph Series*, pp. 83–105.

27. J. M. Warren, L. N. Hansen, Ductile Deformation of the Lithospheric Mantle. *Annu. Rev. Earth Planet. Sci.* **51**, 581–609 (2023).

28. G. F. Davies, Mechanics of subducted lithosphere. *J. Geophys. Res. Solid Earth* **85**, 6304–6318 (1980).

29. C. R. Bina, Patterns of deep seismicity reflect buoyancy stresses due to phase transitions. *Geophys. Res. Lett.* **24**, 3301–3304 (1997).

30. A. Mohiuddin, S. Karato, An experimental study of grain-scale microstructure evolution during the olivine–wadsleyite phase transition under nominally "dry" conditions. *Earth Planet. Sci. Lett.* **501**, 128–137 (2018).

31. Y. Fukao, M. Obayashi, T. Nakakuki, the Deep Slab Project Group, Stagnant Slab: A Review. *Annu. Rev. Earth Planet. Sci.* **37**, 19–46 (2009).

32. U. R. Christensen, D. A. Yuen, Layered convection induced by phase transitions. *J. Geophys. Res. Solid Earth* **90**, 10291–10300 (1985).

33. P. J. Tackley, D. J. Stevenson, G. A. Glatzmaier, G. Schubert, Effects of an endothermic phase transition at 670 km depth in a spherical model of convection in the Earth's mantle. *Nature* **361**, 699–704 (1993).

34. M. I. Billen, G. Hirth, Rheologic controls on slab dynamics. *Geochem. Geophys. Geosystems* **8** (2007).

35. H. Čížková, C. R. Bina, Linked influences on slab stagnation: Interplay between lower mantle viscosity structure, phase transitions, and plate coupling. *Earth Planet. Sci. Lett.* **509**, 88–99 (2019).

36. U. R. Christensen, The influence of trench migration on slab penetration into the lower mantle. *Earth Planet. Sci. Lett.* **140**, 27–39 (1996).

37. S. Yoshioka, A. Naganoda, Effects of trench migration on fall of stagnant slabs into the lower mantle. *Phys. Earth Planet. Inter.* **183**, 321–329 (2010).

38. W. B. Durham, S. Mei, D. L. Kohlstedt, L. Wang, N. A. Dixon, New measurements of activation volume in olivine under anhydrous conditions. *Phys. Earth Planet. Inter.* **172**, 67–73 (2009).

39. N. A. Dixon, W. B. Durham, Measurement of Activation Volume for Creep of Dry Olivine at Upper-Mantle Conditions. *J. Geophys. Res. Solid Earth* **123**, 8459–8473 (2018).

40. Y. Wang, W. B. Durham, I. C. Getting, D. J. Weidner, The deformation-DIA: A new apparatus for high temperature triaxial deformation to pressures up to 15 GPa. *Rev. Sci. Instrum.* **74**, 3002–3011 (2003).

41. D. J. Weidner, M. T. Vaughan, L. Wang, H. Long, L. Li, N. A. Dixon, W. B. Durham, Precise stress measurements with white synchrotron x rays. *Rev. Sci. Instrum.* **81**, 013903 (2010).

42. L. N. Hansen, K. M. Kumamoto, C. A. Thom, D. Wallis, W. B. Durham, D. L. Goldsby, T. Breithaupt, C. D. Meyers, D. L. Kohlstedt, Low-Temperature Plasticity in Olivine: Grain Size, Strain Hardening, and the Strength of the Lithosphere. *J. Geophys. Res. Solid Earth* **124**, 5427–5449 (2019).

43. R. M. Goddard, K. M. Kumamoto, L. N. Hansen, D. Wallis, A. J. Cross, C. A. Thom, Validation of subgrain-size piezometry as a tool for measuring stress in polymineralic rocks. ESS Open Archive [Preprint] (2023). https://doi.org/10.22541/essoar.169755254.46171679/v1.

44. A. K. Singh, C. Balasingh, H. Mao, R. J. Hemley, J. Shu, Analysis of lattice strains measured under nonhydrostatic pressure. *J. Appl. Phys.* **83**, 7567–7575 (1998).

45. E. H. Abramson, J. M. Brown, L. J. Slutsky, J. Zaug, The elastic constants of San Carlos olivine to 17 GPa. *J. Geophys. Res. Solid Earth* **102**, 12253–12263 (1997).

46. D. G. Isaak, High-temperature elasticity of iron-bearing olivines. *J. Geophys. Res. Solid Earth* **97**, 1871–1885 (1992).

47. Z. Mao, D. Fan, J.-F. Lin, J. Yang, S. N. Tkachev, K. Zhuravlev, V. B. Prakapenka, Elasticity of single-crystal olivine at high pressures and temperatures. *Earth Planet. Sci. Lett.* **426**, 204–215 (2015).

48. I. Suzuki, Thermal Expansion of Periclase and Olivine, and Their Anharmonic Properties. *J. Phys. Earth* **23**, 145–159 (1975).

49. J. Girard, R. E. Silber, A. Mohiuddin, H. Chen, S. Karato, Development of a Stress Sensor for In-Situ High-Pressure Deformation Experiments Using Radial X-Ray Diffraction. *Minerals* **10**, 166 (2020).

50. B. Lafuente, R. T. Downs, H. Yang, N. Stone, "The power of databases: The RRUFF project" in *Highlights in Mineralogical Crystallography* (2015), pp. 1–29.

51. P. Raterron, S. Merkel, C. W. Holyoke III, Axial temperature gradient and stress measurements in the deformation-DIA cell using alumina pistons. *Rev. Sci. Instrum.* **84**, 043906 (2013).

52. T. Nagai, O. Ohtaka, T. Yamanaka, Kinetic studies of the α-quartz-coesite transformation of SiO2. *Mineral. J.* **19**, 147–154 (1997).

53. T. Nagai, S. Mori, O. Ohtaka, T. Yamanaka, Nucleation and Growth Kinetics of the a-Quartz-Coesite Transformation Using both Powder and Single Crystal Samples. *Rev. High Press. Sci. Technol.* **7**, 125–127 (1998).

54. H. Morishima, T. Kato, M. Suto, E. Ohtani, S. Urakawa, W. Utsumi, O. Shimomura, T. Kikegawa, The Phase Boundary Between α- and β-Mg2SiO4 Determined by in Situ X-ray Observation. *Science* **265**, 1202–1203 (1994).

Acknowledgments: The authors thank Leif Tokle and Amanda Dillman for providing the quartz and olivine starting materials, respectively. AJC acknowledges salary support from the Investment in Science Program (ISP) and Assistant Scientist Endowment Support (ASES) programs at WHOI. Use of the Advanced Photon Source, Argonne National Laboratory, was supported by the U.S. Department of Energy, Office of Science, Office of Basic Energy Sciences, under Contract No. DE-AC02-06CH11357. Use of the 6BM-B beamline was supported by COMPRES, the Consortium for Materials Properties Research in Earth Sciences, under NSF Cooperative Agreement EAR 16-06856. Portions of this work were performed under the auspices of the U.S. Department of Energy by Lawrence Livermore National Laboratory under Contract DE-AC52-07NA27344. LLNL-JRNL-859365.

Funding:
National Science Foundation grant EAR-2023128 (AJC, DLG, LNH)
National Science Foundation grant EAR-2003389 (AJC)
National Science Foundation grant EAR-1806791 (KMK)

Author contributions:
Conceptualization: AJC, DLG
Funding Acquisition: AJC, DLG, LNH
Investigation: AJC, RMG, KMK, HC, DH, CAT, AN, LNH, DLG,
Formal Analysis: AJC, DH
Software: KMK, LNH, AJC
Writing - Original Draft Preparation: AJC
Writing - Review & Editing: AJC, RMG, KMK, DLG, LNH, HC, DH, AN

Competing interests: Authors declare that they have no competing interests.

Data and materials availability: All data and code necessary to understand and assess the conclusions of this manuscript have been uploaded as Supplementary Materials.

Supplementary Materials:
Materials and Methods
Supplementary Text
Figs. S1 to S9
Tables S1 to S4
Data S1 to S13

Supplementary Materials for

Synchrotron radiation reveals transient weakening during mineral phase transformations

Andrew J. Cross[1]*, Rellie M. Goddard[1,2], Kathryn M. Kumamoto[3], David L. Goldsby[4], Lars N. Hansen[5], Haiyan Chen[6], Diede Hein[5], Christopher A. Thom[7], M. Adaire Nehring[5]

[1] Department of Geology and Geophysics, Woods Hole Oceanographic Institution; Woods Hole, MA 02532, USA
[2] Department of Geology, Lakehead University; Thunder Bay, ON P7B 5E1, Canada
[3] Lawrence Livermore National Laboratory; Livermore, CA 94550, USA
[4] Department of Earth and Environmental Science, University of Pennsylvania; Philadelphia, PA 19104, USA
[5] Department of Earth and Environmental Sciences, University of Minnesota, Twin Cities; Minneapolis, MN 55455, USA
[6] Mineral Physics Institute, Stony Brook University; Stony Brook, NY 11794, USA
[7] Rhenium Alloys, Inc.; North Ridgeville, OH 44035, USA

*Corresponding author. Email: across@whoi.edu

The PDF file includes:

Materials and Methods
Supplementary Text
Figs. S1 to S9
Tables S1 to S4

Other Supplementary Materials for this manuscript include the following:

Data S1 to S13

Materials and Methods

Starting Materials

Dense polycrystalline aggregates of quartz (SiO_2) were prepared via isostatic hot-pressing of natural quartz sand with 5-μm particle size and >99.5% purity (Min-U-Sil® 5, U.S. Silica Corp.). Quartz powders were loaded into a Hot Isostatic Press apparatus at ETH Zurich, and hot-pressed for 36 hours at 1200°C and 200 MPa gas confining pressure. No water was added to the powders prior to hot-pressing. After hot-pressing, samples were cored to 1.10 ± 0.05 mm diameter, and ground to 0.50 ± 0.05 mm height. The mean grain size of the hot-pressed quartz starting material, "LT-QHP", was 7.0 ± 3.9 μm, determined via electron backscatter diffraction (EBSD) mapping at the Marine Biological Laboratory (Woods Hole, MA). In two early experimental runs (San467, San468), we observed a 4–8% net volume loss within the SiO_2 sample following a two-way traverse of the quartz-coesite phase boundary, which we attribute to pore collapse in the hot-pressed quartz starting material. In all subsequent experiments, we first cold-pressed the sample at room temperature and ~5 GPa confining pressure (to close any pores) before depressurizing to our desired starting pressure of 1–2 GPa. X-ray diffraction (XRD) spectra were collected during some of these cold-presses to verify that the SiO_2 sample remained metastable as quartz.

Each sample assembly also contained a dense polycrystalline aggregate of hot-pressed San Carlos olivine ($(Mg_{0.9}Fe_{0.1})_2SiO_4$), which was primarily used to calculate stress and pressure *in situ* via energy-dispersive XRD (details provided below). However, the olivine aggregate also served as a control sample since it does not undergo any phase transformations over the range of experimental conditions explored here. San Carlos powders with particle size <10 μm containing ~1% orthopyroxene were dried at 1000°C for 12 hours in a gas-mixing furnace with oxygen fugacity set to ~10^{-7} Pa. Next, the powders were cold-pressed into a Ni capsule, loaded into a Paterson gas-medium apparatus, and vacuum hot-pressed for 1 hour at 1200–1250°C and 300 MPa confining pressure with a vacuum pressure of 10–27 Pa on the interior of the capsule. After hot-pressing, samples were cored and ground to 1.10 ± 0.05 mm diameter and 0.50 ± 0.05 mm height, respectively. Olivine samples were extracted from three such hot-presses: PI-2056, PI-2094 and PT-1616. We note that the powder used for hot-press PI-2094 had a light-gray discoloration, presumably arising from Fe contamination during ball-milling. However, Fe contamination should not affect the elastic properties of olivine. Portions of each hot-press were polished using diamond lapping film down to a grit size of 0.5 μm and finished with a vibratory colloidal silica polish. Polished samples were coated with 5 nm carbon and examined via EBSD at the University of Minnesota on a JEOL JSM 6500F field emission gun scanning electron microscope (FEG-SEM) operating in high-vacuum mode at an accelerating voltage of 20 kV. EBSD maps were collected at step-sizes of 0.5 μm (PI-2056) or 0.1 μm (PI-2094, PT-1616). These maps revealed mean grain sizes (calculated as area-equivalent diameters) of 6.6 ± 3.7 μm, 3.3 ± 1.0 μm and 2.2 ± 1.9 μm for PI-2056, PI-2094 and PT-1616, respectively.

Sample Assembly

All experimental assemblies contained one quartz sample and one olivine sample stacked in series (*i.e.*, on top of one another; Fig. S1). Dense alumina and machinable alumina pistons were placed above and below the stacked samples, with thin Ni disks separating each component for the purpose of tracking axial strain (*i.e.*, sample height) via X-ray radiography. To monitor sample diameter and thereby calculate volumetric strain, the stacked samples were also wrapped in Ni foil. The Ni foil and disks also served to fix oxygen fugacity near the Ni/NiO buffer. The stacked samples and pistons were inserted into a cylindrical MgO sleeve, which itself was contained within a cylindrical graphite resistance heater ("furnace"), a mullite sphere, and a soft-fired pyrophyllite cube with edges 6.1–6.35 mm in length (Fig. S1). The mullite sphere and pyrophyllite cube served as pressure media and provided a dry environment for the samples (*38*), which were not sealed. After assembly, the components were cemented in place with ZrO_2 paste and dried overnight at 100°C. The assembly did not contain a thermocouple to avoid introducing a source of mechanical instability at high pressure. Instead, temperature was determined using either 1) a calibrated relationship between temperature and furnace power, or 2) the flow strength of olivine and/or the kinetics of the quartz→coesite phase transformation. These methods provide minimal loss of accuracy given the inherently large thermal gradients within the small sample assembly (*39*). Details on the temperature calibration are provided below.

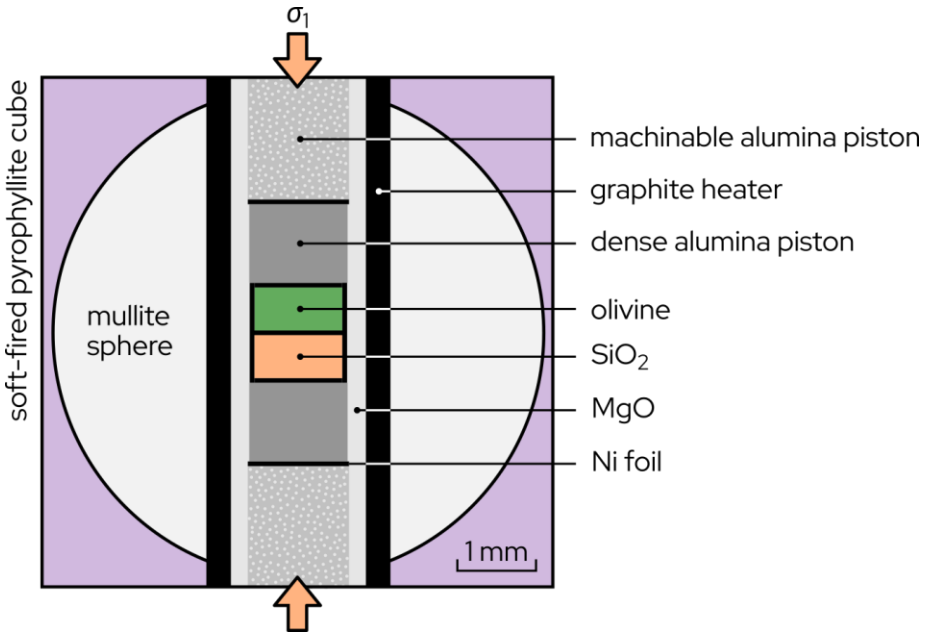

Fig. S1. Schematic diagram of the D-DIA cell assembly. Polycrystalline aggregates of olivine and SiO_2 are stacked in series along the maximum principal stress (σ_1) direction.

Apparatus Details

Experiments were performed in a Deformation-DIA (D-DIA) apparatus (*40*) located on beamline sector 6-BM-B of the Advanced Photon Source synchrotron (Argonne National Laboratory, Chicago, IL). The D-DIA apparatus consists of three orthogonal pairs of anvils sandwiched between an upper and lower guide block, with each anvil in contact with one face of the sample assembly cube. Confining pressure is generated by advancing the main hydraulic ram, which changes the separation distance between the upper and lower guide blocks, advancing the six anvils equally. Meanwhile, deviatoric stress conditions can be imposed by independently moving the vertical pair of anvils, termed "differential rams". Differential ram motion is controlled by advancing (or retracting) a pair of hydraulic syringe pumps at a specified rate. Constant syringe pump motion does not perfectly translate into constant strain-rate conditions due to compressibility of the hydraulic fluid. Rather, strain rate evolves to steady-state over a period of a few percent strain following each change in experiment conditions (for example, at the start of each experiment, or following a phase transformation). Experiment conditions are summarized in Table S1.

In Situ Stress, Strain, and Phase Proportion Measurements

Throughout each experiment, synchrotron X-ray radiation was used to calculate stress and quartz-coesite volume proportions via energy-dispersive XRD, and axial and volumetric strain via X-ray radiography. The detector geometry and procedures for calculating stress and strain have been described in detail elsewhere (*39*, *41*–*43*). In short, XRD data were obtained by directing a 100 × 100 μm white X-ray beam through a gap between the upstream horizontal anvils, into the sample assembly. Diffraction spectra were collected at a downstream array of 10 solid-state detectors arranged at fixed azimuths of $\Psi = 0$–$270°$ with respect to the horizontal incident beam—see Figure 3 in (*39*). The detectors, along with a set of conical slits, were positioned such that the X-ray beam was collimated to a Bragg angle of $2\theta \approx 6.5°$. The precise Bragg angle was calibrated approximately once every three experiments (*i.e.*, once per day) using a powdered alumina standard. Each XRD energy peak corresponds to a (*hkl*) plane for which the lattice spacing, d_{HKL}, is obtained using Bragg's law. Changes in *d*-spacing under load (*i.e.*, lattice strain) provide quantitative constraints on the stress state of a sample via its elastic properties. During uniaxial shortening in the D-DIA, for instance, lattice strain should be greatest in the (horizontal) plane normal to the shortening axis, and smallest in any (vertical) plane containing the shortening axis. Thus, differential stress is given by the difference in d_{HKL} at $\Psi = 0°$ and $\Psi = 90°$ via the Singh *et al.* (*44*) formulation of Hooke's law, which assumes an isostress condition. In this study, differential stress was calculated separately for the (130), (131), and (112) planes in olivine, using the elastic constants for olivine from Abramson *et al.* (*45*), along with their pressure derivatives (*45*) and temperature derivatives (*46*). Meanwhile, mean stress was calculated using a third-order Birch-Murnaghan equation of state for olivine, with values of 129.4 GPa and 4.29 for the olivine bulk modulus and its pressure derivative, respectively (*45*),

−0.02 GPa/K for the olivine bulk modulus temperature derivative (*47*), and the thermal expansivity of olivine from Suzuki (*48*). Note that in this study we draw a distinction between confining pressure, $P = \sigma_3$, and mean stress, $\sigma_m = (\sigma_1 + 2\sigma_3)/3$, wherein we assume that $\sigma_2 = \sigma_3$, given the axisymmetric deformation geometry. Differential stress is given as $\sigma_d = \sigma_1 - \sigma_3$, for which positive values indicate deviatoric compression, and negative values indicate deviatoric tension, assuming that σ_1 (σ_3) is given by the lattice strain along the vertical (horizontal) axis in the deformation apparatus, parallel (perpendicular) to the uniaxial shortening axis.

Diffraction patterns were collected with dwell times of 5–30 seconds, alternating between the olivine and SiO_2 samples. We calculated stresses and pressures only for olivine, assuming the stress states in the stacked olivine and SiO_2 samples to be the same—previous workers have shown this to be a reasonable assumption within experimental uncertainty (*42*, *43*, *49*). Due to the plastic anisotropy of olivine, there is some variation in stress measured using the different lattice planes. The average range in stress varies from 60–210 MPa for our experiments, with the (130) peak consistently giving the largest stresses. Previous studies have suggested that the (130) peak provides the most accurate measure of the bulk stress for olivine aggregates in compression (*43*, *49*). SiO_2 diffraction patterns were meanwhile used to monitor the quartz↔coesite phase transformation and estimate the relative volume proportions of those two phases. Volume proportions were calculated using the relative intensities (heights) of peaks belonging to quartz and coesite. Since many of the diffraction peaks in quartz and coesite are weak and overlapping, we limited our analysis to the $(01\bar{1}1)$ peak in quartz, and the (002) and (111) peaks in coesite (Fig. S2). Peaks were tracked in each of the 10 detectors separately, following the subtraction of any background (long wavelength) intensity variation. To account for detector-to-detector variations in signal intensity, each spectrum was also normalized to the range 0–1. Phase volume proportions were calculated for each combination of quartz and coesite peaks as follows:

$$X_C \equiv 1 - X_Q = \frac{I_{Chkl}}{\left(I_{Chkl} + I_{Qhkl}\right)} \quad \textbf{(Eqn. S1)}$$

where X_C and X_Q are the volume fractions of coesite and quartz, respectively, and I is the mean normalized intensity of a particular (*hkl*) peak across all 10 detectors, divided by the maximum expected intensity of that (*hkl*) peak from X-ray powder diffraction (Fig. S2). The subscripts "C" and "Q" denote coesite and quartz, respectively. In practice, the minimum detectable amount of either phase is ~0.75%. Furthermore, in all experiments the two combinations of peaks—$(01\bar{1}1)$ versus (002), and $(01\bar{1}1)$ versus (111)—give estimates within 10% of one another at the 2-sigma level. These sensitivities could be improved by collecting diffraction patterns over longer dwell times; however, we favored short dwell times to provide better temporal resolution during the phase transformations. We should also note that the XRD patterns represent only a 100 × 100 × 1000 μm volume within the center of our samples, corresponding to ~2.5% of the total sample

volume. As such, the measured phase proportions may not be fully representative of the entire sample volume, particularly if the phase transformation is heterogeneous (*e.g.*, due to the heterogeneity of nucleation sites, or thermal gradients within the sample). Indeed, sample volume typically evolves over a longer transient period than the XRD patterns alone would indicate.

Finally, axial and volumetric strain were calculated via digital image cross-correlation of X-ray radiographs collected at 5–30 second intervals throughout each experiment. Interpolation of the X-ray intensity data enabled sub-pixel resolution when tracking the movement of the Ni foils, yielding axial strain resolution down to 10^{-5} and volumetric strain resolution down to 10^{-4}. Volumetric strains were calculated from the two-dimensional X-ray radiographs assuming a cylindrical sample shape, and rotational symmetry of the sample around the compression axis. We estimate that volume strain measurements are accurate within 0–5%, dictated mostly by deviations of the sample from a perfectly cylindrical shape. Axial and volumetric strains are mostly presented here as engineering strains; however, we calculate strain rate and viscosity using true (logarithmic) strains. Shortening strains are reported as positive, while extensional strains are reported as negative.

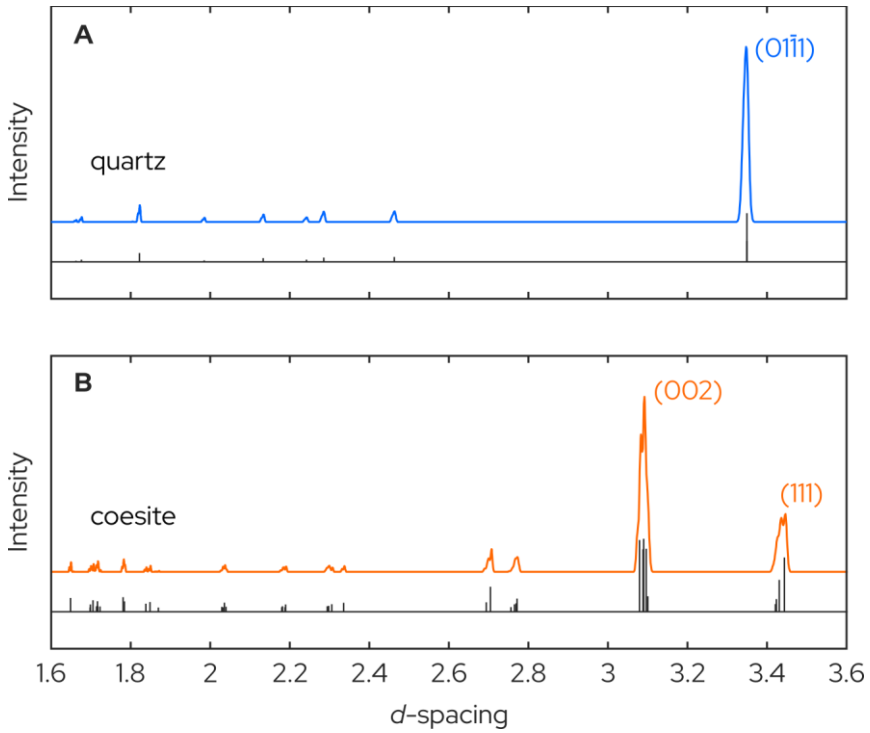

Fig. S2. Calculated X-ray powder diffraction spectra for (A) quartz and (B) coesite. Expected peak positions shown in black. Data from the RRUFF database (ID R100134 and R070565 for quartz and coesite, respectively) (*50*).

Direct Temperature Calibration

The sample assembly used in this study is thermocouple-free for two reasons. First, the presence of a thermocouple introduces mechanical instability, particularly during deformation experiments, due to the large size of the thermocouple relative to the sample assembly. Second, the alumina thermocouple sheath and thermocouple wires act as heat sinks, introducing an additional thermal gradient within the sample assembly—thermal gradients within the small D-DIA assembly volume can exceed 150 K/mm at 1400°C in the presence of a thermocouple (*51*). Instead, we control temperature using a calibration based on the amount of electrical power supplied to the graphite furnace. It has been argued that this approach is at least as accurate as using a thermocouple (*39*), provided that the graphite furnace dimensions and material properties are consistent from assembly to assembly.

The graphite resistance furnaces used in this study were machined at either the University of Oxford, UK (experiments San467–San574) or the University of Minnesota Twin Cities, USA (experiments San585–San652). We hereafter refer to these as "Oxford" and "UMN" furnaces. To determine the power-temperature relationship of our furnaces, we performed a calibration run (San658) using a UMN furnace. Temperature was measured at the center of the sample assembly using a thermocouple (Fig. S3A–B), and monitored as a function of 1) furnace power and 2) the amount of hydraulic load acting on the main ram over a range of 10–50 tons (for context, the experiments described in this paper were conducted at 10–40 tons).

We find a modest effect of load on the temperature-power relationship. Between 10 and 30 tons, the graphite furnace becomes more efficient with increasing load—in other words, the furnace power required to reach a given temperature decreases—whereas from 30 to 50 tons, the graphite furnace becomes less efficient with increasing load (Fig. S3C). Interestingly, there is also an apparent memory effect, such that furnace efficiency does not evolve with subsequent decreases in load below the maximum attained load, F_m (Fig. S3D). We therefore define a calibration containing two independent variables: furnace power, P (in watts), and the maximum previous load experienced by the sample assembly, F_m (in tons):

$$T_{cal} = B_1 {F_m}^3 + B_2 P {F_m}^2 + B_3 P^2 F_m + B_4 P^3 + B_5 {F_m}^2 + B_6 P F_m + B_7 P^2 + B_8 F_m + B_9 P + B_{10} \quad \textbf{(Eqn. S2)}$$

where $B_1 = 4.44 \times 10^{-3}$, $B_2 = -1.20 \times 10^{-4}$, $B_3 = -3.56 \times 10^{-6}$, $B_4 = -3.37 \times 10^{-6}$, $B_5 = -0.453$, $B_6 = 4.10 \times 10^{-3}$, $B_7 = 4.46 \times 10^{-3}$, $B_8 = 13.6$, $B_9 = 2.96$, and $B_{10} = -61.9$. This fit produces residuals of ± 20°C at the 2-sigma level, compared to residuals of ± 30°C when the load effect is ignored. Conveniently, with the exception of San467 and San468, all other experiments began with a ~5 GPa (40 ton) *in situ* cold press (as described above), such that the maximum load was

set at the beginning of each experiment. Furnace efficiency (and, thus, temperature) should have therefore been constant throughout each experiment, regardless of the imposed changes in load.

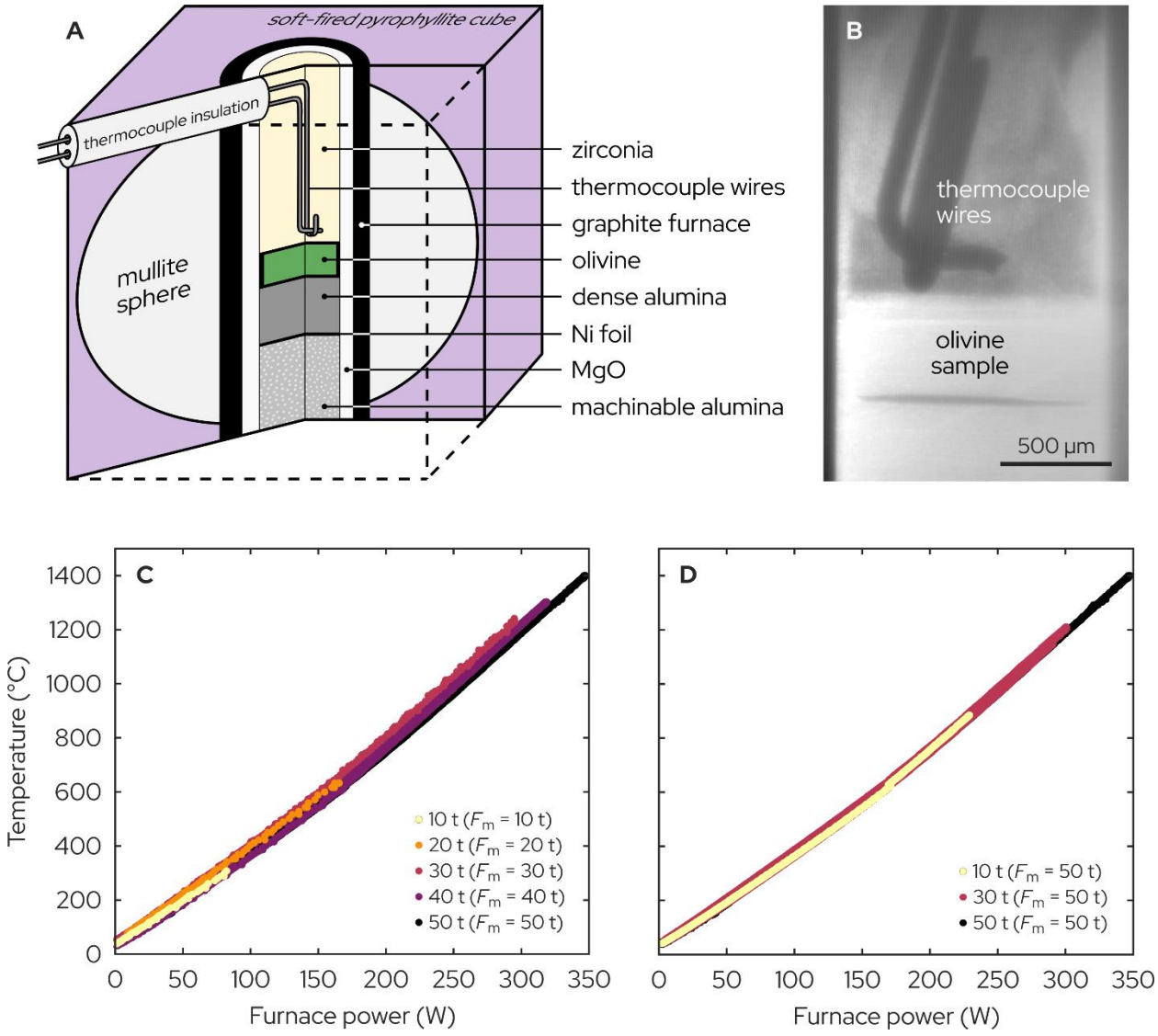

Fig. S3. UMN furnace calibration. (**A**) Cell assembly for the furnace calibration. (**B**) X-ray radiograph showing the position of the thermocouple near the cell center. (**C–D**) Temperature versus furnace power. Colors correspond to the main ram load at which each set of measurements was made. During increments of increasing load, the power-temperature relationship changes (**C**); however, when load is subsequently decreased, the power-temperature relationship no longer evolves (**D**) and is set according to the maximum load previously experienced by the sample assembly, F_m.

Indirect Temperature Calibration—Quartz↔Coesite Transformation Kinetics

Despite being machined to the same nominal dimensions, the UMN and Oxford furnaces do not appear to follow the same power-temperature relationship. First, experiments performed with Oxford furnaces at 167 W furnace power—San537, San538, San558—are weaker than experiments performed with UMN furnaces at 209 W furnace power and comparable strain rates—San585, San588, San652 (Fig. 2). Second, the quartz↔coesite transformation is significantly quicker in the experiments with Oxford furnaces compared to the experiments with UMN furnaces. We therefore infer that experiments San537, San538, and San558 (Oxford furnaces), were actually hotter than experiments San585, San588, and San652 (UMN furnaces), despite the latter operating at greater furnace power.

In the absence of a suitable power-temperature calibration, we require other means for estimating temperature in experiments containing Oxford furnaces. We tackle this using two independent analyses: the steady-state flow strength of olivine, and the kinetics of the quartz-to-coesite phase transformation.

The quartz→coesite transformation kinetics have already been determined at experimental conditions very similar to ours by Nagai *et al.* (*52*, *53*). First, we refit their data to the Avrami equation (Fig. S4):

$$X = 1 - \exp(-kt^m) \qquad \textbf{(Eqn. S3)}$$

$$k = k_0 \exp(-Q/RT) \qquad \textbf{(Eqn. S4)}$$

where X is the fraction of transformed material, t is time, m is the dimensionless Avrami exponent, and k is a rate parameter expressed as a function of a pre-exponential constant, k_0, the activation enthalpy of the transformation, Q, the gas constant, R, and absolute temperature, T. This formulation does not account for pressure (or, rather, overpressure). We infer that pressure effects are minimal since the Nagai *et al.* (*52*, *53*) experiments were performed at confining pressures of either 4 or 6 GPa—that is, with either ~1 or ~3 GPa of overstepping—yet conform reasonably well to a single Avrami fit (Fig. S4).

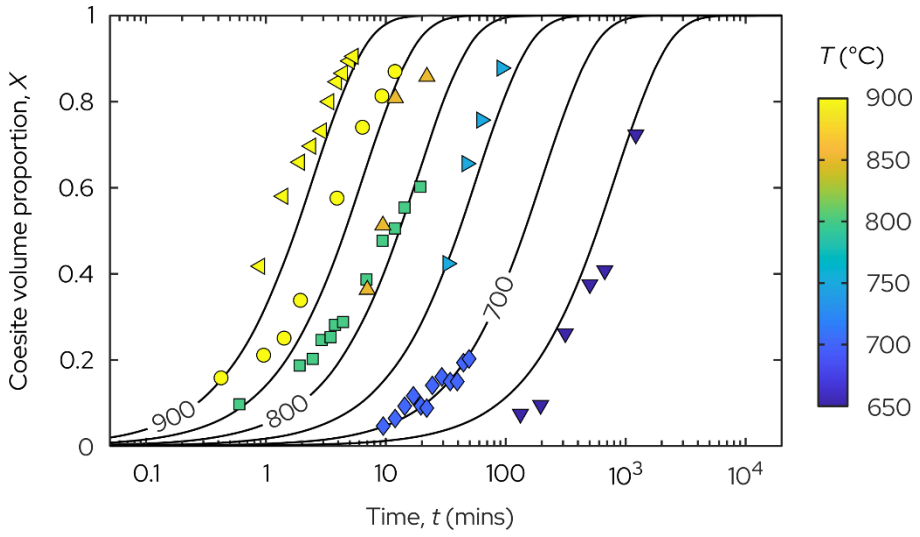

Fig. S4. Quartz→coesite transformation kinetics. Data are from Nagai *et al.* (1997, 1998), colored according to temperature, and refit using Eqns. S3–S4 with $n = 1$.

As in Nagai *et al.* (*52*, *53*), we fix the Avrami exponent at $n = 1$, which yields values of $\log_{10}(k_0) = 16.38$ (± 1.40) s^{-1}, and $Q = 209$ (± 12) kJ mol^{-1}, where the uncertainties are given as two standard deviations. Next, we fit our quartz→coesite phase proportion data to the Avrami equation (Eqn. S3) to obtain the rate parameter, k, for each experiment, while again fixing $n = 1$. A "kinetics temperature", T_{kin}, is then obtained for each experiment via Eqn. S4, using the values of k_0 and Q derived from the Nagai *et al.* (*52*, *53*) data. To estimate the uncertainty on each kinetics temperature, we perform a Monte Carlo analysis where we generate 10^6 random values of the parameters $\log_{10}(k)$, $\log_{10}(k_0)$, and Q, each following a Gaussian distribution of width dictated by the 2-sigma uncertainty for each parameter. These randomly generated values are then used to calculate a range of T_{kin} for each experiment. At the 2-sigma level, these temperatures consistently vary within an uncertainty range of ± 50–60°C. The rate parameters, kinetics temperatures, and temperature uncertainties are summarized in Table S2.

Encouragingly, we note that the UMN-furnace experiments (San585, San588, San652) yield kinetics temperatures (784°C, 805°C, 836°C, respectively) that are remarkably close to the temperature estimated from the UMN power-temperature calibration, 810 ± 20°C, with a mean offset of only −2°C. Moreover, the Oxford-furnace experiments described above (San537, San538, San558) yield kinetics temperatures that are indeed higher (870°C, 841°C, 828°C, respectively), despite the lower furnace power in those experiments, as inferred above.

Indirect Temperature Calibration—Olivine Flow Strength

For comparison against the kinetics temperatures described above, we also calculate "flow law temperatures", T_{flow}, using olivine flow laws of the following general form:

$$\dot{\varepsilon}_i = A_i \, \sigma^{n_i} \, d^{-m_i} \exp\left(-\frac{E_i + PV_i}{RT}\right) \quad \textbf{(Eqn. S5)}$$

where $\dot{\varepsilon}$ is the steady-state strain rate, A is a pre-exponential constant, σ is differential stress, n is the stress exponent, d is grain size, m is the grain-size exponent, E is activation energy, P is confining pressure, V is activation volume, R is the gas constant, T is absolute temperature, and the subscript "i" indicates parameters determined for the ith deformation mechanism. Here, we assume that the total creep rate of our olivine sample is given as:

$$\dot{\varepsilon} = \dot{\varepsilon}_{dis} + \dot{\varepsilon}_{GBS} + \dot{\varepsilon}_{dif} \quad \textbf{(Eqn. S6)}$$

where the subscripts "dis", "GBS", and "dif" represent dislocation creep, dislocation-accommodated grain boundary sliding (disGBS), and diffusion creep, respectively.

To calculate T_{flow}, we take our steady-state stresses (and corresponding pressures over the same time intervals)—in addition to the parameters for dry dislocation creep, dry disGBS, and dry diffusion creep of olivine, as summarized by Warren & Hansen (*27*)—and systematically vary T to find the total strain rate, $\dot{\varepsilon}$, that best matches our measured steady-state strain rates (Table S3). For each steady-state point, we obtain three T_{flow} values using the stresses and pressures calculated from the olivine (130), (131), and (112) diffraction peaks. Furthermore, for each experiment we obtain steady-state measurements at up to three points: during initial deformation within the quartz stability field, during deformation within the coesite stability field, and during final deformation back in the quartz stability field. Thus, we derive up to nine T_{flow} values for each experiment (see Table S3).

Because our XRD stress measurements are calculated using the elastic constants of olivine (and their pressure and temperature derivatives), we must assume some initial value of temperature for the XRD calculations. We therefore perform an iterative process in which an initial temperature estimate (900°C) is used to calculate stress and pressure from the XRD data. These stresses and pressures are used to derive an initial T_{flow} estimate for the Oxford-furnace experiments (via Eqns. S5 and S6). The XRD data are then reprocessed using that initial T_{flow} estimate—which also depends on T_{kin} as described below—to obtain refined stress, pressure, and T_{flow} values. For San588, which we take as a representative experiment, we find that the T_{flow} converges (within 5°C; *i.e.*, 0.5%) after only two iterations of this process. We therefore perform only two iterations for every experiment containing an Oxford furnace. Furthermore, we

converge upon the same stresses (within 5 MPa; *i.e.*, 0.5%), pressures (within 0.15 GPa; *i.e.*, 25%), and T_{flow} values (within 5°C; *i.e.*, 0.5%) even when varying the initial temperature estimate by ± 500°C.

In Fig. S5, we compare our derived values of T_{kin} and T_{flow}. Reassuringly, we find a positive correlation between the two. Furthermore, we emphasize that these temperature estimates are entirely independent—T_{kin} is based on XRD peak intensity in the SiO_2 sample, whereas T_{flow} is derived from XRD peak position in the olivine sample. However, while the kinetics temperatures appear entirely reasonable—as stated above, the experiments with UMN furnaces yield T_{kin} values remarkably close to the temperature expected from our UMN furnace calibration ($T_{cal\text{-}UMN}$ = 810°C)—our T_{flow} values seem unrealistically high. First, the experiments with UMN furnaces give T_{flow} values that are 190–560°C (20–65%) higher than the temperature expected from the UMN furnace calibration (red points in Fig. S5A). Second, some experiments with Oxford furnaces yield T_{flow} values that approach the melting point of our Ni strain markers (1450–1650°C over the range of pressures explored here). In other experiments using the same D-DIA apparatus, cell assembly, and materials (*42*, *43*), we routinely imposed furnace power values of up to 280 W (*i.e.*, >30%, or nominally >300°C, greater than that applied here) without melting the Ni markers. At this time, we do not know the cause of the unrealistically high T_{flow} values. Although we have neglected the role of low-temperature plasticity in our T_{flow} calculations (Eqns. 5–6), the experiments that give the highest T_{flow} values exhibit very low differential stresses (<100 MPa), with minimal work hardening. Thus, the contribution of low-temperature plasticity in most experiments is likely negligible. Water is also an unlikely culprit. With wet olivine flow laws, we would have to invoke water concentrations far exceeding the water solubility of olivine to obtain T_{flow} values consistent with our T_{kin} values and calibrated temperatures. Finally, our differential stress—and, thus, T_{flow}—calculations are only minimally sensitive to temperature uncertainties. For example, varying the XRD data-processing temperature by ± 200°C causes T_{flow} to vary by no more than ± 30°C for San588.

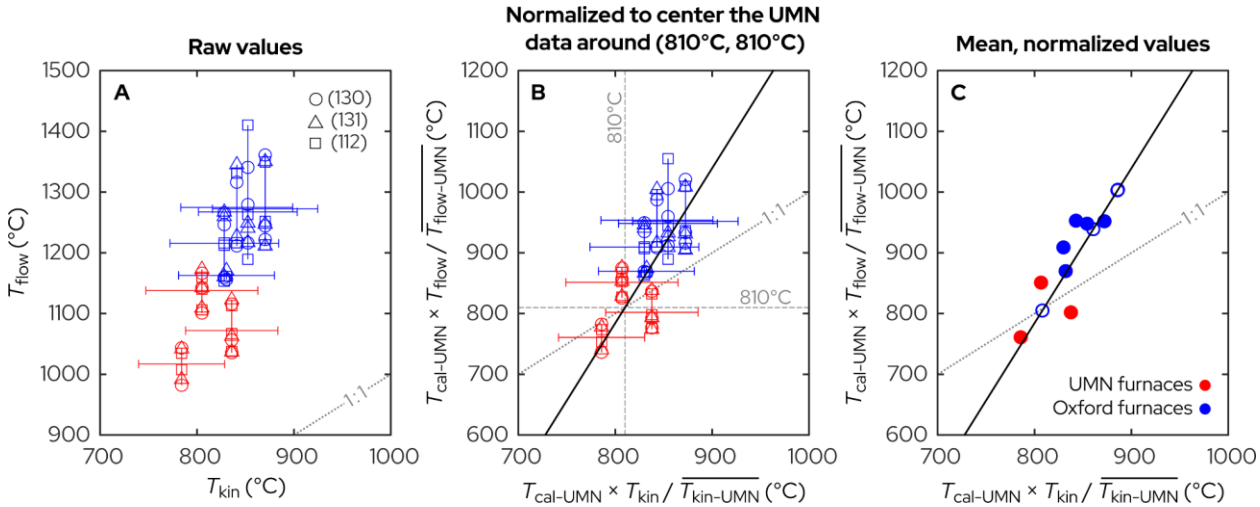

Fig. S5. Comparison of temperatures derived from the olivine flow law, T_{flow}, and temperatures derived from the quartz→coesite transformation kinetics, T_{kin}. (**A**) Raw values. (**B**) Values normalized by the average T_{kin} and T_{flow} values of the UMN-furnace experiments (red points), and then rescaled to center the UMN-furnace experiments around their calibrated temperature, $T_{cal\text{-}UMN}$ = 810°C, derived from our UMN furnace calibration (Eqn. S2). The black line shows a linear regression through the data (black line), which is forced to pass through $T_{cal\text{-}UMN}$ = 810°C. (**C**) The mean normalized values for each experiment. Solid symbols indicate experiments where both T_{kin} and T_{flow} are constrained. Hollow symbols indicate experiments where either T_{kin} and T_{flow} could not be constrained—in these cases, we estimate the missing temperature using the linear regression (solid black line) derived in (**B**).

To resolve the discrepancy between T_{kin} and T_{flow}, we normalize each T_{flow} value by the average T_{flow} value of the UMN-furnace experiments ($\overline{T_{flow-UMN}}$ = 1083°C, 1085°C, and 1080°C, for T_{flow} values obtained from stresses calculated for the (130), (131), and (112) olivine planes, respectively), which were all performed at a furnace power of 209 W. For consistency, we also normalize our T_{kin} values by the average T_{kin} value of the UMN-furnace experiments ($\overline{T_{kin-UMN}}$ = 808°C). We then rescale the normalized values (*i.e.*, convert back to units of degrees Celsius) by multiplying by the calibration temperature of the UMN-furnace experiments, $T_{cal\text{-}UMN}$ = 810°C. The normalized, rescaled data are plotted in Fig. S5B. Note that the UMN-furnace experiments are centered around 810°C (*i.e.*, $T_{cal\text{-}UMN}$).

To obtain a single temperature estimate for each experiment, we take a simple arithmetic average of our mean normalized, rescaled T_{kin} and T_{flow} values (Fig. S5C). However, for some experiments we were unable to determine either T_{kin} (San467, San552, San568) or T_{flow} (San506) due to insufficient data. To aid in constraining the temperature of these experiments, we perform a linear regression through the normalized, rescaled T_{kin} and T_{flow} values, forcing the regression to pass through $T_{cal\text{-}UMN}$ = 810°C (Fig. S5B). The missing temperature is then derived using this relationship (see hollow points in Fig. S5C), which has a root-mean-square misfit of 58°C. We therefore assume that our recalibrated temperatures are accurate to within ± 60°C.

Experiment Procedure

In each experiment, samples were pressurized to 1–2 GPa confining pressure with the differential rams fully retracted (following the ~5 GPa cold press described above). Pressurization typically introduced some differential stress (< 500 MPa), which we relaxed by annealing the samples for 10–30 minutes at 209 W (nominally 800–900°C). XRD patterns were monitored throughout the anneal to verify 1) that the differential stresses became fully relaxed and 2) that the SiO_2 sample remained within the quartz stability field. In non-hydrostatic experiments, the differential rams were then advanced (at the syringe pump rates listed in Table S1) to begin deforming the quartz and olivine samples via uniaxial shortening. Once the quartz and olivine samples were deforming

at a steady state (with the exception of San574, which even after 11% axial strain did not reach state-state), the main ram was steadily advanced to begin increasing the confining pressure. In most experiments, hydraulic load on the main ram was increased at a rate of 0.018–0.037 tons per second, corresponding to a pressure ramp rate of 2–5 MPa/s (Table S1). However, one experiment (San585) was pressurized at ~0.5 MPa/s.

Upon reaching the coesite stability field, we waited for the quartz→coesite transformation to reach completion, and for the SiO_2 and olivine samples to reach steady-state, before reducing pressure to return to the quartz stability field. Note that in both runs performed at our highest deformation rate (0.01 mm/s differential ram syringe pump rate), we stopped the experiments in the coesite stability field to avoid the D-DIA anvils coming into contact due to the large shortening strains reached. In all other experiments, we again waited for the coesite→quartz transformation to reach completion, and for the SiO_2 and olivine samples to reach steady-state, before stopping the experiment. Each experiment was stopped by cutting power to the graphite furnace and stopping the differential rams in quick succession. The load on the main ram was then removed to depressurize the assembly, keeping the differential rams in their advanced position to maintain a small positive deviatoric stress on the sample, and thereby minimize decompression cracking.

Supplementary Text

Viscosity calculation

Viscosity, η (Fig. 2) is calculated as:

$$\eta = \sigma/\dot{\varepsilon} \quad \textbf{Eqn. S7}$$

where σ is differential stress and $\dot{\varepsilon}$ is the true (logarithmic) axial strain rate (hereafter referred to simply as "strain rate"). At each time interval, we obtain three values of viscosity: one for each of the Fo_{90} diffraction peaks, (130), (131), and (112). Strain rate is calculated as the first derivative of true (logarithmic) axial strain with respect to time. However, due to experimental uncertainties on strain, the raw strain-rate measurements are relatively noisy. Therefore, we first smoothed the strain data using a Gaussian-weighted moving average filter. The smoothing window for each experiment varied between 2 and 30 measurements, depending on the length of the experiment and strain rates involved (*i.e.*, larger smoothing windows for long, slow experiments).

Weakening factor (F_W), and rate factor (F_R) calculation

To examine the rate dependence of weakening, we calculate two scaling factors: the weakening factor, F_W, and the rate factor, F_R. The weakening factor is defined as the amplitude of the viscosity drop observed during the quartz→coesite transformation (Fig. 2) or, more explicitly:

$$F_W = \eta_{expected}/\eta_{measured} \quad \textbf{Eqn. S8}$$

where $\eta_{expected}$ is the steady-state viscosity expected for a 50-50 vol.% mixture of quartz and coesite, calculated as the geometric mean of the quartz and coesite viscosities (measured in the steady-state portions of each experiment), while $\eta_{measured}$ is the viscosity measured mid-way through the quartz→coesite transformation. To avoid propagating artifacts introduced by our strain-rate smoothing procedure, we calculate these viscosities using strain rates derived via linear regression through the raw axial strain data. Differential stress is then extracted over the same time interval and used to calculate viscosity (Eqn. S7). For each experiment, we obtain three values of F_W representing the viscosity drop associated with each of the (130), (131), and (112) diffraction peaks in olivine.

The rate factor, F_R, on the other hand, represents the ratio of the transformation rate, $\dot{\varepsilon}_{transform}$, and deformation rate, $\dot{\varepsilon}_{deform}$:

$$F_R = \dot{\varepsilon}_{transform}/\dot{\varepsilon}_{deform} \quad \textbf{Eqn. S9}$$

where $\dot{\varepsilon}_{\text{transform}}$ is taken as the component of the transient volumetric strain rate resolved along the vertical (shortening) direction. More plainly, $\dot{\varepsilon}_{\text{transform}}$ is defined as one third of the volumetric strain rate during the transformation (assuming for simplicity that the quartz→coesite volume change is isotropic). Note, however, that we must first account for the change in volume caused by the change in pressure during the transformation—to achieve this, we divide the pressure ramp rate (in GPa/s) by an assumed average bulk modulus for quartz and coesite of 90 GPa (neglecting elastic softening effects due to the phase transformation for simplicity). We then subtract the resulting volumetric strain rate from the measured (total) volumetric strain rate. The derivation of $\dot{\varepsilon}_{\text{transform}}$ is schematically illustrated in Fig. S6.

Meanwhile, the deformation rate, $\dot{\varepsilon}_{\text{deform}}$, is taken as the geometric mean steady-state strain rate of quartz and coesite; that is, the background strain rate (Fig. S6). Errors on F_{R} are estimated as

$$\Delta F_{\text{R}} = \sqrt{\Delta\dot{\varepsilon}_{\text{transform}}{}^{2} + \Delta\dot{\varepsilon}_{\text{deform}}{}^{2}} \qquad \textbf{Eqn. S10}$$

where Δ denotes error. The transformation rate error, $\Delta\dot{\varepsilon}_{\text{transform}}$, is calculated by conservatively assuming that we can resolve a volumetric strain no smaller than 5×10^{-4} over a typical imaging period of 1 radiograph per 20 seconds (as a reminder, the volumetric strain resolution is 10^{-4})—this yields a volumetric strain rate resolution $\Delta\dot{\varepsilon}_{\text{transform}}$ of 2.5×10^{-4}. Similarly, we conservatively estimate that we can resolve an axial strain of no less than 5×10^{-5} over a period of 20 seconds (the axial strain resolution is actually 10^{-5}), providing an axial strain rate resolution, $\Delta\dot{\varepsilon}_{\text{deform}}$ of 2.5×10^{-5}. These values are both larger than the observed noise floor of our strain-rate measurements, verifying that they are indeed conservative estimates of the strain rate uncertainty. Eqn. S10 further ensures an upper estimate on ΔF_{R} since it assumes constructive superposition of $\Delta\dot{\varepsilon}_{\text{transform}}$ and $\Delta\dot{\varepsilon}_{\text{deform}}$. In reality, these errors are likely negligible for all experiments presented here.

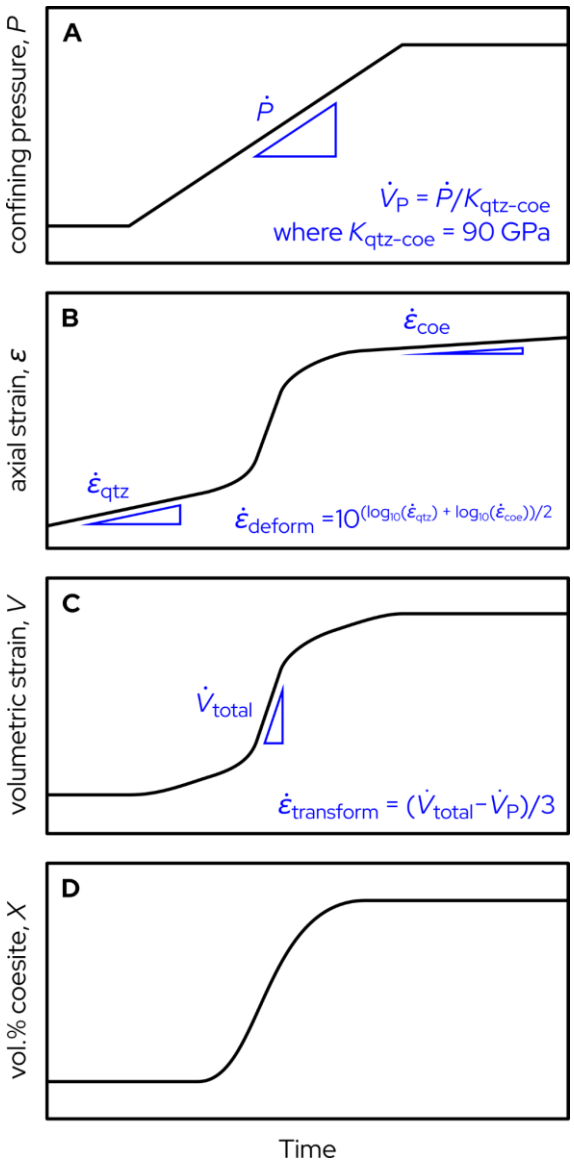

Fig. S6. Derivation of the transformation rate factor, F_R. Schematic plots of (**A**) confining pressure, P, (**B**) axial strain, ε, (**C**) volumetric strain, V, and (**D**) coesite volume fraction, X, as a function of time. F_R represents the ratio between the transformation rate, $\dot{\varepsilon}_{transform}$, and the deformation rate, $\dot{\varepsilon}_{deform}$ (Eqn. S9). $\dot{\varepsilon}_{deform}$ is given as the geometric mean of the steady-state strain rates of quartz and coesite (**B**). Meanwhile, $\dot{\varepsilon}_{transform}$ is given as one third of the volumetric strain rate during the transformation, $\dot{V}_{total}$ (**C**), minus the volumetric strain rate due to the imposed change in pressure, $\dot{V}_P$ (**A**). In principle, $\dot{\varepsilon}_{transform}$ represents an effective axial strain rate due to the quartz→coesite volume change.

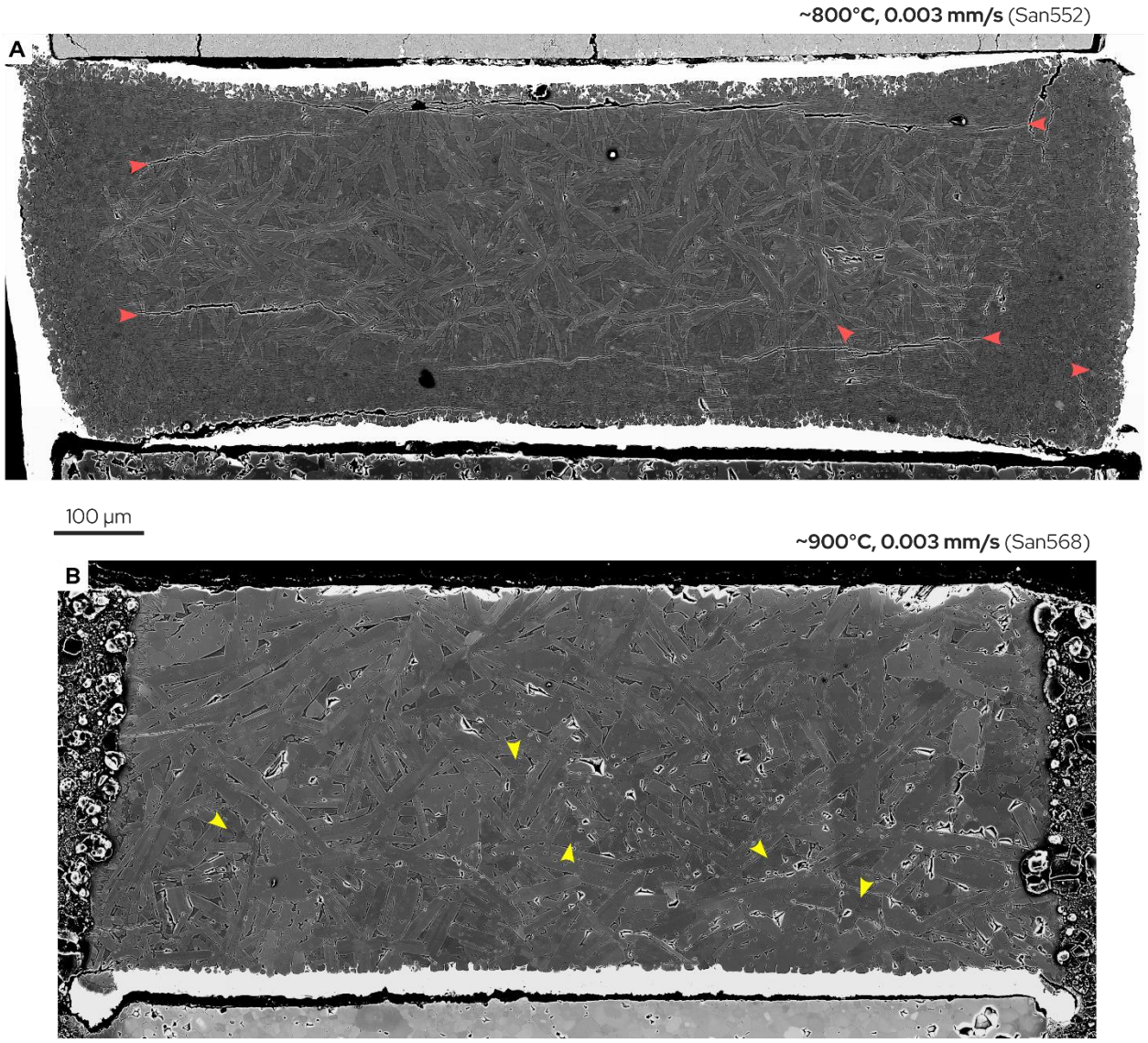

Fig. S7. Microstructure of samples quenched mid-way through the quartz→coesite phase transformation under non-hydrostatic conditions. Backscatter electron (BSE) images collected using a Zeiss Supra 40VP FEG-SEM at the Marine Biological Laboratory, Woods Hole, MA. (A) Sample San552, conducted at ~800°C and 0.003 mm/s differential ram syringe pump rate (~50% coesite), and (B) sample San568, conducted at ~900°C and also 0.003 mm/s differential ram syringe pump rate (~90% coesite). The shortening direction is vertical for both samples. The lighter phase is coesite; the darker phase is quartz. Red arrows indicate decompression cracks, while yellow arrows indicate remnant quartz grains in San568.

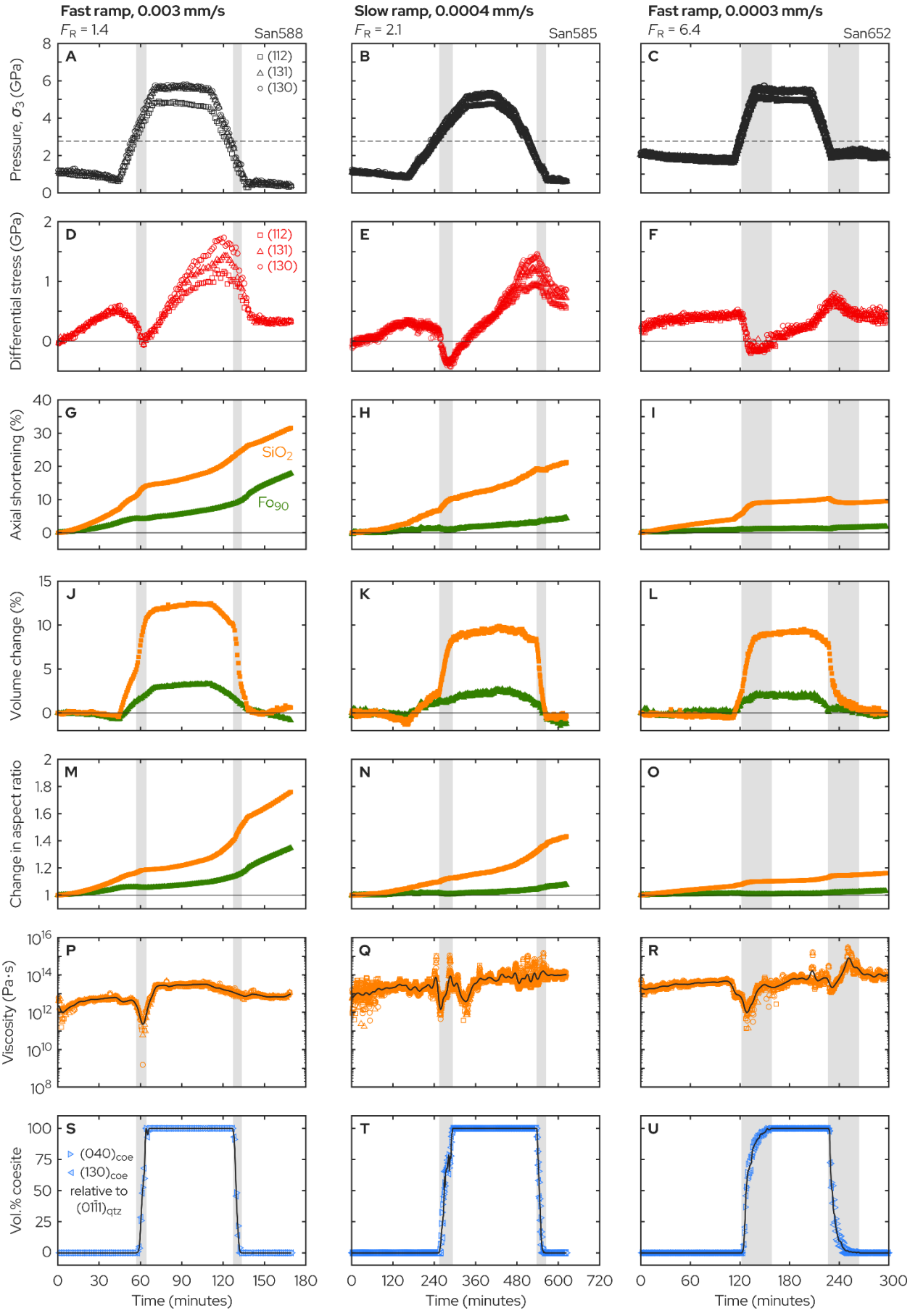
Fast ramp, 0.003 mm/s
F_R = 1.4
San588
Slow ramp, 0.0004 mm/s
F_R = 2.1
San585
Fast ramp, 0.0003 mm/s
F_R = 6.4
San652
A
B
C
(112)
(131)
(130)
Pressure, σ_3 (GPa)
D
E
F
Differential stress (GPa)
G
H
I
SiO_2
Fo_{90}
Axial shortening (%)
J
K
L
Volume change (%)
M
N
O
Change in aspect ratio
P
Q
R
Viscosity (Pa·s)
S
T
U
$(040)_{coe}$
$(130)_{coe}$
relative to
$(01\bar{1}1)_{qtz}$
Vol.% coesite
Time (minutes)
Time (minutes)
Time (minutes)

Fig. S8. Effect of pressure ramp rate on transformational weakening. (**A–C**) Confining pressure, σ_3, (**D–F**) differential stress, $\sigma_1-\sigma_3$, (**G–I**) axial strain, (**J–L**) volumetric strain, (**M–O**) sample aspect ratio (diameter divided by width) relative to the initial sample shape, (**P–R**) viscosity, and (**S–U**) coesite volume proportion as a function of time. Vertical gray bars represent the time intervals over which both quartz and coesite peaks are present in the XRD spectra. Orange squares and green triangles represent the SiO_2 sample and Fo_{90} reference standard, respectively, in (**G–O**). As a visual aid, a spline has been fit through the average of the viscosity and volume proportion data in (P–U; black curves) All experiments were performed at graphite furnace powers corresponding to a nominal temperature of 810°C. Pressure was ramped at a rate of 2.2–3.2 MPa/s in San588 (left column) and San652 (right column), and 0.4–0.6 MPa/s in San585 (middle column). The differential ram syringe pump rate (*i.e.*, deformation rate) is indicated in units of mm/s above each column. The rate ratio, F_R (transformation rate divided by deformation rate) increases from left to right.

Slab model

To explore the likelihood of transformational weakening on geological timescales, we calculate the transformation and deformation rates of a downgoing slab passing through the mantle transition zone (Fig. S9). Following Hosoya *et al.* (*23*), we calculate the progression of the olivine-wadsleyite phase transformation for a slab descending at a rate of 12 cm/yr, with a thermal gradient of 0.6 K/km. The volume fraction of transformed material, X, is calculated as

$$X = 1 - \exp\left[2S \int \dot{x}(z)\, dz\right] \qquad \textbf{Eqn. S11}$$

where S is the grain boundary area of the parent phase, olivine (taken as $3.35/d$, where d is the grain size of olivine), and $\dot{x}(z)$ is the growth rate at each increment of depth, z, given by

$$\dot{x} = BTC_{\mathrm{OH}}{}^{p} \exp\left(-\frac{E_g + PV_g}{RT}\right)\left[1 - \exp\left(-\frac{\Delta E_r}{RT}\right)\right] \qquad \textbf{Eqn. S12}$$

where B is a pre-exponential rate factor, T is absolute temperature, C_{OH} is water content in wt. ppm H_2O, p is the water exponent of the phase transformation, E_g is the activation energy for growth of the product phase (wadsleyite), P is pressure, V_g is the activation volume for growth, R is the gas constant, and ΔE_r is the free energy change of the transformation (taken as $\Delta P \Delta V$, where ΔP is the overpressure relative to the phase boundary, and ΔV is the difference in specific volume between the parent and product phase). Overpressure is calculated as the difference between the pressure at any given depth and the pressure expected for the olivine-wadsleyite

phase boundary at corresponding pressure-temperature conditions. Pressure is calculated using the relation $P = \rho g z$ (where ρ is density and g is gravitational acceleration), while the phase boundary is defined as $P = 9.3 + 0.0036T$, with temperature, T, in units of degrees Celsius (*54*). The kinetic parameter values, boundary conditions, and model constants are provided in Table S4.

Meanwhile, we calculate deformation rates in the downgoing slab using rheological flow laws for olivine. Given the relatively low temperatures, high stresses, and coarse olivine grain size, it is assumed that deformation proceeds via low-temperature plasticity and dislocation creep:

$$\dot{\varepsilon}_{\mathrm{deform}} = \dot{\varepsilon}_{\mathrm{LTP}} + \dot{\varepsilon}_{\mathrm{dis}} \qquad \textbf{Eqn. S13}$$

$$\dot{\varepsilon}_{\mathrm{LTP}} = A_{\mathrm{LTP}}\, \rho_{\mathrm{d}} \exp\left(-\frac{E_{\mathrm{LTP}}}{RT}\right) \sinh\left(\frac{E_{\mathrm{LTP}}}{RT}\frac{\sigma - \sigma_{\mathrm{p}}}{\Sigma}\right) \qquad \textbf{Eqn. S14}$$

$$\dot{\varepsilon}_{\mathrm{dis}} = A_{dis}\, \sigma^{n}\, {C_{\mathrm{OH}}}^{r} \exp\left(-\frac{E_{dis} + PV_{dis}}{RT}\right) \qquad \textbf{Eqn. S15}$$

where the subscripts "LTP" and "dis" denote low-temperature plasticity and dislocation creep, respectively, $\dot{\varepsilon}$ is strain rate, A is a pre-exponential rate constant, ρ_{d} is dislocation density, E is activation energy, σ is differential stress, σ_{p} is the backstress due to long-range dislocation interactions, Σ is the Peierls stress, n is the stress exponent, and r is the water exponent. For low-temperature plasticity, we use a flow law of the form proposed by Hansen *et al.* (*42*), with parameters applicable to the onset of plastic deformation—that is, at the yield point, prior to work hardening and the development of a backstress. Note that we use these parameters because steady-state low-temperature plasticity is expected only for applied stresses exceeding 1.8 GPa, whereas slab stress estimates are on the order of a few hundred MPa at most (*28–30*). For dislocation creep, we use the wet flow law parameters from Hirth & Kohlstedt (*26*) with the revised A value from Warren & Hansen (*27*). The flow law parameters are provided in Table S4.

At each given depth, X is calculated and converted to a volumetric strain (Fig. S9A) assuming that there is a 10% density increase (*i.e.*, 10% volume contraction) associated with the olivine-wadsleyite phase transition. By taking the first time derivative of the true (logarithmic) volumetric strain, we obtain the volumetric strain rate as a function of depth. As above, the transformation rate, $\dot{\varepsilon}_{\mathrm{transform}}$ (Fig. S9B) is taken as one third of the volumetric strain rate (to obtain the effective strain rate produced by the transformation along the direction of maximum principal stress), assuming for simplicity that the volume change is isotropic. Meanwhile, we calculate the deformation rate, $\dot{\varepsilon}_{\mathrm{deform}}$, as a function of depth using Eqns. S13–S15 (Fig. S9C).

For each combination of temperature, water content, and stress boundary conditions, we obtain a single value of the rate factor, F_R—that is, the ratio of the transformation and deformation rates—by finding the peak transformation rate (Fig. S9B, black arrow) and then taking the deformation rate at the same depth (Fig. S9C, black arrow). In the example provided in Fig. S9, we obtain a maximum value for $\dot{\varepsilon}_{transform}$ of 1.0×10^{-15} s^{-1}, and $\dot{\varepsilon}_{deform}$ = 1.2×10^{-18} s^{-1} at the same depth (550 km), giving a rate factor value of F_R = 830 for this set of conditions (600°C slab temperature at the 660 km discontinuity, 2000 wt. ppm H_2O, 300 MPa differential stress).

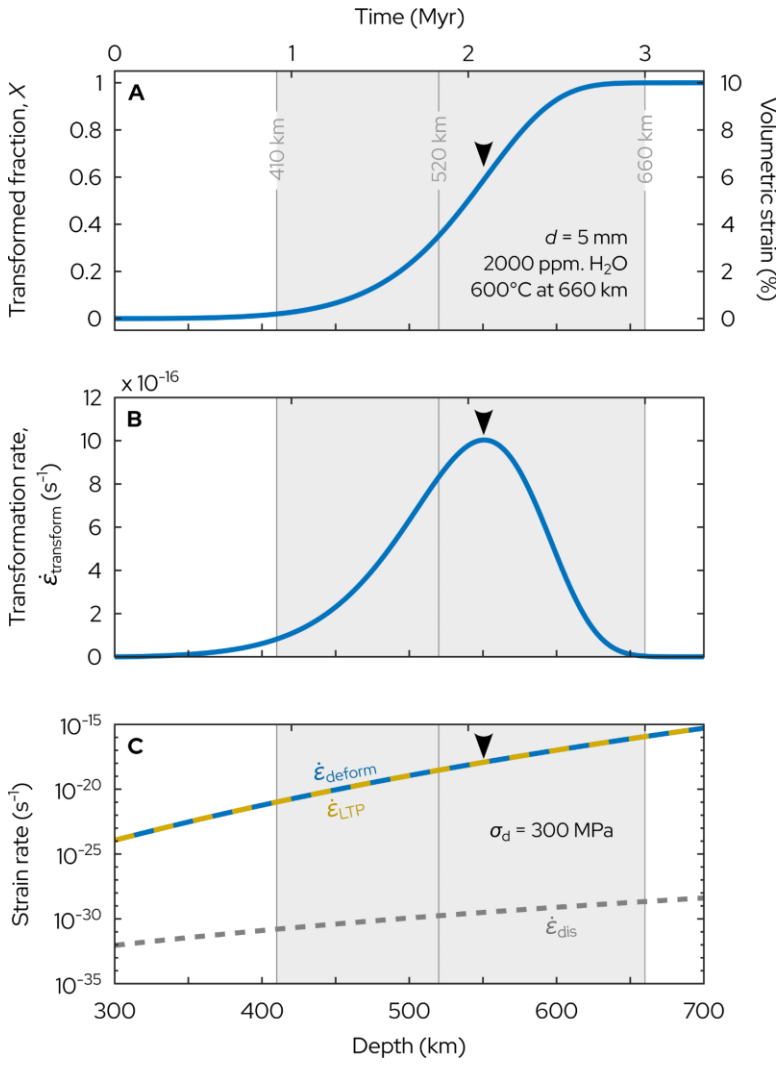

Fig. S9. Model of transformation and deformation rates in a downgoing slab. (**A**) Volume fraction of material transformed from olivine to wadsleyite, *X*, and the associated volumetric strain, as a function of depth. (**B**) First derivative of the volumetric strain from (**A**), divided by three to obtain the effective strain rate produced by the transformation along the direction of maximum principal stress (assuming that the volume change is isotropic). (**C**) Olivine strain rate, $\dot{\varepsilon}_{deform}$, given as the sum of the strain rates due to low-temperature plasticity (subscript "LTP") and dislocation creep (subscript "dis") as a function of depth, for a differential stress of 300 MPa.

621 **Table S1.** Experiment run conditions

Experiment #	Top sample	Bottom sample	Graphite furnace origin	Furnace power (W)	Temperature (°C)	Differential ram syringe pump rate (mm/s)	Pressure ramp rate, up / down (MPa/s)	Rate factor, F_R	Weakening factor, F_W		
									(112)	(131)	(130)
Hydrostatic ($\sigma_1 \approx \sigma_2 \approx \sigma_3$)											
San506	PI-2056	LT-QHP	Oxford	188	945†	0	2.6 / 2.7	N/A	N/A	N/A	N/A
Non-hydrostatic ($\sigma_1 > \sigma_2 \approx \sigma_3$)											
San467*	PI-2056	LT-QHP	Oxford	209	944†	0.003	4.6 / 3.6	4.4 ± 0.12	99	97	25
San537	LT-QHP	PI-2056	Oxford	167	892†	0.003	2.6 / 2.9	2.3 ± 0.18	16	14	26
San538	LT-QHP	PI-2056	Oxford	167	903†	0.01	3.1 / N/A	0.48 ± 0.19	0.72	0.67	0.64
San558	PI-2094	LT-QHP	Oxford	167	869†	0.0003	2.8 / 3.3	15 ± 0.96	39	28	26
San572	PI-2094	LT-QHP	Oxford	198	851†	0.01	2.5 / N/A	0.49 ± 0.25	0.48	0.47	0.48
San574	PI-2094	LT-QHP	Oxford	209	901†	0.0003	2.6 / 2.4	99 ± 4.4	49	47	46
San585	LT-QHP	PT-1616	UMN	209	810‡	0.0004	0.41 / 0.60	2.1 ± 1.2	11	7.9	7.6
San588	PT-1616	LT-QHP	UMN	209	810‡	0.0003	3.1 / 3.2	1.4 ± 0.25	13	11	14
San652	PT-1616	LT-QHP	UMN	209	810‡	0.003	2.4 / 2.2	6.4 ± 1.0	105	23	28
Mid-transformation quench (non-hydrostatic)											
San552	PI-2094	LT-QHP	Oxford	209	807†	0.003	1.3 / N/A	N/A	N/A	N/A	N/A
San568	LT-QHP	PI-2094	Oxford	209	900†	0.003	2.9 / N/A	N/A	N/A	N/A	N/A

* Experiment performed without initial room-temperature pressure cycle (see Materials and Methods for details)

† Temperature inferred from the quartz⟶coesite transformation kinetics and/or olivine flow strength (see Materials and Methods for details). ± 60°C uncertainty.

‡ Temperature calculated using power-temperature calibration (Fig. S3; Eqn. S2). ± 20°C uncertainty.

622

Table S2. Temperature calibration data—quartz→coesite transformation kinetics

Experiment #	Olivine sample	Graphite furnace origin	Furnace power (W)	Avrami rate parameter, k (s^{-1})	Temperature estimate, T_{kin} (°C)
Hydrostatic ($\sigma_1 \approx \sigma_2 \approx \sigma_3$)					
San506	PI-2056	Oxford	188	4.89×10^{-3}	884 ± 52
Non-hydrostatic ($\sigma_1 > \sigma_2 \approx \sigma_3$)					
San467*	PI-2056	Oxford	209	-	-
San537	PI-2056	Oxford	167	3.76×10^{-3}	870 ± 54
San538	PI-2056	Oxford	167	2.11×10^{-3}	841 ± 58
San558	PI-2094	Oxford	167	1.62×10^{-3}	828 ± 56
San572	PI-2094	Oxford	198	1.70×10^{-3}	830 ± 49
San574	PI-2094	Oxford	209	2.65×10^{-3}	852 ± 51
San585	PT-1616	UMN	209	6.27×10^{-4}	784 ± 44
San588	PT-1616	UMN	209	9.95×10^{-4}	805 ± 58
San652	PT-1616	UMN	209	1.90×10^{-3}	836 ± 48
Mid-transformation quench (non-hydrostatic)					
San552*	PI-2094	Oxford	209	-	-
San568*	PI-2094	Oxford	209	-	-

* Not enough data points for Avrami regression

Table S3. Temperature calibration data—olivine flow law

Experiment #	Graphite furnace origin	Olivine sample	Furnace power (W)	Phase*	Steady-state strain rate, olivine (s^{-1})	Steady-state differential stress (MPa)			Confining pressure (GPa)			Temperature estimate, T_{flow} (°C)		
						(112)	(131)	(130)	(112)	(131)	(130)	(112)	(131)	(130)
Non-hydrostatic ($\sigma_1 > \sigma_2 \approx \sigma_3$)														
San467	Oxford	PI-2056	209	quartz-1	7.94×10^{-6}	50	89	−41	1.68	1.71	2.00	1388	1333	-
				coesite†	6.97×10^{-6}	-	-	-	-	-	-	-	-	-
				quartz-2	2.46×10^{-5}	119	152	183	1.56	1.75	1.84	1350	1329	1311
San537	Oxford	PI-2056	167	quartz-1	1.70×10^{-5}	322	365	378	2.30	2.51	2.54	1252	1247	1244
				coesite	1.57×10^{-5}	415	524	489	5.39	6.04	6.13	1350	1350	1361
				quartz-2	1.29×10^{-5}	295	310	291	1.45	1.53	1.61	1213	1211	1222
San538	Oxford	PI-2056	167	quartz-1	1.29×10^{-5}	449	455	534	2.57	2.85	2.88	1217	1227	1212
				coesite	3.15×10^{-5}	681	819	1065	5.57	6.42	6.42	1332	1345	1316
San558	Oxford	PI-2094	167	quartz-1	3.69×10^{-6}	115	64	51	2.00	2.84	2.34	1213	1267	1266
				coesite	1.10×10^{-8}	10	19	15	5.72	7.38	6.88	1154	1161	1160
				quartz-2	3.83×10^{-6}	67	45	45	0.89	1.71	1.21	1216	1260	1247
San572	Oxford	PI-2094	198	quartz-1†	8.91×10^{-5}	-	-	-	-	-	-	-	-	-
				coesite	2.24×10^{-5}	1106	1353	1611	3.47	4.20	4.22	1161	1171	1156
San574	Oxford	PI-2094	209	quartz-1	2.00×10^{-6}	18	25	15	1.18	1.35	1.45	1263	1249	1280
				coesite	-1.19×10^{-6}	−324	−261	−285	5.25	5.99	6.14	1189	1217	1216
				quartz-2	1.88×10^{-6}	1	23	4	0.81	0.92	1.03	1411	1241	1341

Table S3 cont.

Experiment #	Graphite furnace origin	Olivine sample	Furnace power (W)	Phase*	Steady-state strain rate, olivine (s^{-1})	Steady-state differential stress (MPa)			Confining pressure (GPa)			Temperature estimate, T_{flow} (°C)		
						(112)	(131)	(130)	(112)	(131)	(130)	(112)	(131)	(130)
San585	UMN	PT-1616	209	quartz-1	1.31×10^{-6}	344	305	306	0.83	0.84	0.9	1035	1042	1043
				coesite†	1.07×10^{-6}	-	-	-	-	-	-	-	-	-
				quartz-2	1.97×10^{-6}	585	737	858	0.62	0.63	0.66	1008	992	982
San588	UMN	PT-1616	209	quartz-1	2.19×10^{-5}	482	490	545	0.66	0.78	0.79	1106	1109	1101
				coesite	1.12×10^{-5}	980	1198	1401	4.62	5.52	5.63	1160	1173	1166
				quartz-2	2.98×10^{-5}	324	326	334	0.39	0.47	0.52	1140	1143	1143
San652	UMN	PT-1616	209	quartz-1	9.21×10^{-7}	397	424	453	1.66	1.76	1.84	1038	1037	1036
				coesite	4.70×10^{-7}	222	220	271	4.95	5.41	5.47	1113	1123	1116
				quartz-2	1.49×10^{-7}	359	427	485	1.92	2.1	2.12	1067	1063	1056
Mid-transformation quench (non-hydrostatic)														
San552	Oxford	PI-2094	209	quartz-1	1.34×10^{-5}	977	1185	1367	1.63	1.99	2.00	1083	1080	1068
San568	Oxford	PI-2094	209	quartz-1	1.49×10^{-5}	168	69	111	1.07	1.07	1.27	1221	1286	1259

* "quartz-1" indicates deformation during the initial stage in the quartz stability field; "coesite" indicates deformation in the coesite stability field; "quartz-2" indicates deformation during the final stage in the quartz stability field

† Steady-state not reached

Table S4. Slab model parameters

Parameter	Description	Value	Units
Boundary conditions and constants			
Z	depth	variable	m
dT/dz	thermal gradient	0.6×10^{-3}	K/m
dz/dt	subduction rate	0.12	m/yr
T_{660}	absolute temperature at 660 km discontinuity	873–1473	K
C_{OH}	water content	1–10000	wt. ppm H_2O
σ	differential stress	1–300	$\times 10^6$ Pa
ρ	density	3600*	kg/m^3
g	gravitational acceleration	9.81	m/s^2
P	pressure	$\rho g z$	Pa
R	gas constant	8.314	J mol^{-1} K^{-1}
Olivine-wadsleyite phase transformation (intercrystalline nucleation and growth)†			
d	grain size of parent phase	0.005	m
S	grain boundary area of parent phase	$3.35/d$	m^2/m^3
B	pre-exponential rate constant	exp(−18)	m s^{-1} K^{-1} wt. ppm H_2O^{-p}
p	water exponent	3.2	-
E_g	activation energy	274	$\times 10^3$ J/mol
V_g	activation volume	3.3	$\times 10^{-6}$ m^3/mol
ΔV	change in specific volume	3.0‡	$\times 10^{-6}$ m^3/mol
ΔE_r	free energy change	$\Delta P/\Delta V$	J/mol
Olivine deformation, low temperature plasticity§			
A_{LTP}	pre-exponential rate constant	$10^{-1.32}$	m^2/s
ρ_d	dislocation density	10^{10}	m/m^3
E_{LTP}	activation enthalpy	450	$\times 10^3$ J/mol
σ_p	backstress	0	$\times 10^6$ Pa
Σ	Peierls stress	3100	$\times 10^6$ Pa

631 **Table S4 cont.**

Parameter	Description	Value	Units
Olivine deformation, wet dislocation creep¶			
A_{dis}	pre-exponential rate constant	570#	s^{-1} Pa^{-n} wt. ppm H_2O^{-p}
n	stress exponent	3.5	-
r	water exponent	1.2	-
E_{dis}	activation energy	480	$\times 10^3$ J/mol
V_{dis}	activation volume	11	$\times 10^{-6}$ m^3/mol

* Density of San Carlos olivine at ~12 GPa (*45*)
† Values from Hosoya *et al.* (*23*) unless stated otherwise
‡ Values from Mohiuddin & Karato (*30*)
§ Values from Warren & Hansen (*27*)
¶ Values from Hirth & Kohlstedt (*26*) unless stated otherwise
# As revised by Warren & Hansen (*27*)

632
633
634 **Data S1–S12.** Mechanical data (separate files). Comma-separated value (CSV) files with the
635 time (column A), confining pressure (B–C), differential stress (E–G), SiO_2 sample shape (H–J),
636 SiO_2 axial strain (K), SiO_2 volumetric strain (L), Fo_{90} stress sensor shape (M–O), Fo_{90} axial
637 strain (P), Fo_{90} volumetric strain (Q), and coesite volume percentages (R–S) for each experiment
638 listed in Table 1. Pressures, stresses, and phase proportions were obtained from X-ray
639 diffraction, while sample strains were obtained via X-ray radiography. Diffraction spectra and
640 radiographs were collected alternately.
641
642 **Data S13.** Slab model (separate file). MATLAB® model used to investigate the transformation
643 kinetics and strain rates of olivine during descent in a downgoing slab (Figs. 4 and S9). Written
644 and tested using MATLAB® version R2022b. See *Supplementary Text* for full description.